A 3D Shear Velocity Model of the Crust and Uppermost Mantle Beneath the United States from Ambient Seismic Noise

G. D. Bensen

Center for Imaging the Earth's Interior, Department of Physics, University of Colorado at Boulder, Boulder, Colorado USA

M. H. Ritzwoller

Center for Imaging the Earth's Interior, Department of Physics, University of Colorado at Boulder, Boulder, Colorado USA

Y. Yang

Center for Imaging the Earth's Interior, Department of Physics, University of Colorado at Boulder, Boulder, Colorado USA

G. D. Bensen, Department of Physics, University of Colorado at Boulder, Campus Box 390, Boulder, CO 80309, USA. (gbensen@colorado.edu)

Abstract.

In an earlier study, *Bensen et al.* [2008] measured surface wave dispersion curves from ambient noise using 203 stations across North America, which resulted in Rayleigh and Love wave dispersion maps from 8 - 70 s period and 8 - 20 s period, respectively. We invert these maps in a two-step procedure to determine a three-dimensional (3D) shear wave velocity model (V_s) of the crust and uppermost mantle beneath much of the contiguous US. The two steps are a linearized inversion for a best fitting model beneath each grid node, followed by a Monte-Carlo inversion to estimate model uncertainties. In general, a simple model parameterization is sufficient to achieve acceptable data fit, but a Rayleigh/Love discrepancy at periods from 10 to 20 sec is observed in which a simple isotropic model systematically misfts Rayleigh and Love waves in some regions. Crustal features observed in the model include sedimentary basins such as the Anadarko, Green River, Williston Basins as well as California's Great Valley and the Mississippi Embayment. The east-west velocity dichotomy between the stable eastern US and the tectonically deformed western US is shown to be abrupt in the crust and uppermost mantle, but is not coincident in these regions; crustal high velocity material tends to lap over the high velocities of the uppermost mantle. The Rayleigh/Love discrepancy between 10 and 20 sec period is crustal in origin and is observed in a number of regions, particularly in extensional provinces such as the Basin and Range. It can be resolved by introducing radial anisotropy in the lower or middle crust with $Vsh > Vsv$ by about 1%.

1. Introduction

Seismic tomography on both global and regional scales has been performed in recent years covering all or part of the continental United States. The resulting models, however, have had either limited geographic extent or relatively low resolution. Recent studies have shown that surface wave ambient noise tomography (ANT) helps to fill the gap between regional and continental or global scale tomographic models (e.g., *Shapiro et al.* [2005], *Yao et al.* [2006], *Moschetti et al.* [2007], *Lin et al.* [2007], *Yang et al.* [2007a]). Nevertheless, constraints from ANT on 3D models of the crust and uppermost mantle have been applied mainly at regional scales (e.g., *Yang et al.* [2007a], *Yao et al.* [2006]). We show that ANT can be applied to produce 3D structural information at the continental scale and that ANT helps to diminish the typical resolution/coverage trade-off that characterizes earthquake based studies on this scale. Seismic data now emerging from Earthscope's USArray provide the potential for further improvement in resolution for which our model may serve as a useful reference.

This study is an extension of work presented by *Bensen et al.* [2007] and *Bensen et al.* [2008]. *Bensen et al.* [2007] presented a technique for computing reliable empirical Green's functions (EGF) from long sequences of ambient noise. They also presented an automated procedure to measure the dispersion of EGFs as well as selection criteria to ensure that only high-quality signals are retained. Using these methods, *Bensen et al.* [2008] estimated maps of Rayleigh and Love wave group and phase speed across the US. Using 203 stations across North America (labeled as black triangles in Figure 1) for up to two years of ambient noise data, they developed surface wave dispersion maps on a 0.5° x 0.5° grid.

They constructed dispersion maps from 8 - 70 s period for Rayleigh waves and 8 - 20 s period for Love waves. These dispersion maps form the basis for the current study. Aspects of the work by *Bensen et al.* [2007] and *Bensen et al.* [2008] are summarized here as appropriate.

Regional investigations of surface wave propagation and dispersion in the United States date back over 30 years (e.g., *Lee and Solomon* [1978]). Tomographic studies using increasing volumes of data in the US (e.g., *Alsina et al.* [1996], *van der Lee and Nolet* [1997], *Godey et al.* [2003], *Li et al.* [2003], *Marone et al.* [2007], *Nettles and Dziewonski* [2008]) have presented dispersion maps and models that have been improving resolution over similar studies at global scales (e.g., *Trampert and Woodhouse* [1996], *Ekström et al.* [1997], *Ritzwoller et al.* [2002]). A large number of regional studies also have been performed to investigate the seismic structure of North America. Among these are tomographic studies in regions such as the Rio Grande Rift (e.g., *Gao et al.* [2004]), Cascadia (e.g., *Ramachandran et al.* [2005]), California (e.g., *Thurber et al.* [2006]), the Rocky Mountains (e.g., *Yuan and Dueker* [2005]) and the eastern US (e.g., *van der Lee* [2002]), to name a few recent studies among many others. Many refraction studies have provided profiles across North America, including CD-ROM (e.g., *Karlstrom et al.* [2002]), Deep Probe (e.g., *Snelson et al.* [1998]) and others. Receiver functions have provided valuable constraints on crustal thickness and structure in parts of the continent (e.g., *Crotwell and Owens* [2005]).

ANT complements these methods and possesses several features that commend its use. First, within the context of a seismic array, high path density can be achieved with paths contained entirely within the study region, minimizing bias from structures outside the region of interest. Second, station locations are known precisely, unlike earthquake locations. Third, phase velocity measurements from ambient noise are free from an initial source phase (*Lin et al.* [2007]), which reduces uncertainty compared with earthquake derived measurements. Fourth, ambient noise dispersion measurements are repeatable, which allows measurement uncertainties to be estimated (*Bensen et al.* [2008]). Fifth, the bandwidth of ambient noise dispersion measurements (i.e., 6 - 100 s period) constrains the structure both of the crust and uppermost mantle. In contrast, it is difficult across much of the US to obtain earthquake based surface wave dispersion measurements below ~15 s period. Previous surface wave studies, therefore, obtained high-quality dispersion measurements predominantly at longer periods and, therefore, reported velocity structure predominantly in the mantle (e.g., *Shapiro and Ritzwoller* [2002], *van der Lee and Frederiksen* [2005], *Nettles and Dziewonski* [2008]). Body wave studies of similar geographic extent also provide only weak constraints on crustal structure(e.g., *Grand* [1994], *Grand* [2002]).

The 3D model derived here will be useful to improve earthquake locations in some regions, aid receiver function studies, and provide a starting model for other investigations across the US. This may be especially important in the context of the advancing USArray/Transportable Array experiment.

2. Data

The data used in this study are the Rayleigh and Love wave group and phase speed dispersion maps from *Bensen et al.* [2008]. These maps are based on Rayleigh and Love wave group and phase speed dispersion measurements obtained from EGFs computed between the stations shown in Figure 1. Dispersion measurements are made on EGFs created by cross-correlating long ambient noise time series using the data processing and measurement techniques described in detail by *Bensen et al.* [2007] and *Lin et al.* [2007]. Nearly 20,000 paths are used for this experiment and up to 13 unique measurements from different temporal subsets of the two-year time series along each path are computed for each wave type. Measurement uncertainties are estimated from the repeatability of the measurements across the temporal subsets. An automated Frequency Time Analysis (FTAN) is used to measure the dispersion of these Rayleigh and Love wave signals (*Levshin et al.* [1972], *Bensen et al.* [2007]). *Bensen et al.* [2008] developed acceptance criteria to ensure that only EGFs of high quality are retained. Starting with nearly 20,000 paths across the United States and Canada, a maximum of 8,932 paths remained after selection. The result was group and phase speed tomography maps for Rayleigh waves between 8 and 70 s period and between 8 and 20 s for Love waves. Low signal quality for Love waves at longer periods causes the narrower bandwidth and apparently results from higher local noise on horizontal components, particularly in the eastern US. The resulting bandwidth presents sensitivity to shear velocity from the surface into the upper mantle to a depth of about 150 km, as seen in Figure 3. Although uncertainty estimates were presented on the raw dispersion measurements, local uncertainty estimates were not produced on the resulting dispersion maps.

Starting with the set of Rayleigh and Love wave group and phase speed dispersion maps at different periods presented by *Bensen et al.* [2008], we construct local dispersion curves at each point on a 0.5° x 0.5° grid across the US. This process is similar to many previous studies (e.g., *Ritzwoller and Levshin* [1998], *Villaseñor et al.* [2001], *Shapiro and Ritzwoller* [2002], *Weeraratne et al.* [2003], and others).

For the 3D inversion, at each grid point we need an uncertainty value for each period and measurement type. *Bensen et al.* [2008] did not provide this information. *Shapiro and Ritzwoller* [2002] assigned uncertainty based on the overall RMS tomography misfit weighted by resolution. Their uncertainties were geographically invariant except in regions of very low resolution. In our study, there is much more variability in data coverage and quality and we require geographically variable uncertainties. In the interior of the US, much of the uncertainty in the dispersion maps derives from the subjectivity of the choices made in regularization and damping. Near the periphery, however, uncertainty grows due to relatively poorer data coverage and quality.

To address these factors, we create a set of dispersion maps at each period and wave type by varying regularization and smoothing parameters systematically in the inversion (*Barmin et al.* [2001]). The minimum and maximum velocity at each point for each period then define an uncertainty window for that wave type. The uncertainties in the interior of the US, therefore, reflect the confidence in our ability to localize the dispersion information, in contrast with raw measurement errors that reflect the repeatability of the measurements. Within the maps, the regions of greatest uncertainty occur near significant velocity anomalies. The Love wave group speed dispersion curves display much greater variability upon varying regularization and smoothing, and we discard them because of our much lower confidence in their robustness. Finally, we increase uncertainties near the edges of the study region based on estimated resolution which degrades near the edges of the maps. For reference, the 500 km resolution contour for the 16 s Rayleigh wave phase speed map is shown in Figure 2. The mean uncertainty over all periods for the measurements used in this study is shown in Figure 4. The uncertainty values we assign are smaller than RMS tomography misfit values from *Bensen et al.* [2008] at all periods for all wave types, but remain quite conservative.

In performing the Monte-Carlo sampling, we did not vary the Vp/Vs or Vp/ρ ratios. Doing so, mainly affects the model in the upper crust, affecting the mean model minimally but increasing model uncertainty.

In summary, the uncertainties assigned to the dispersion maps are subjective, but, on average, represent our confidence in the maps quantitatively. The uncertainties in the resulting 3D model should be understood in these terms. More rigorous uncertainties will require a different method of surface wave tomography. Fortunately, advances in this direction are on the horizon (e.g., *Lin et al.* [2009]).

3. Methods

Two commonly used methods exist for estimating shear wave velocity structure from surface wave dispersion measurements. The first is linearized waveform fitting as described by *Snieder* [1988], *Nolet* [1990] and others. This technique has been used in many geographical settings with earthquake surface wave signals, including the US (*van der Lee and Nolet* [1997]). The second method, which we adopt, is a two-stage procedure in which period specific 2D tomographic maps created from the dispersion measurements are used first to produce dispersion curves at each geographic grid point. The dispersion curves are then inverted for 1D Vs structure at all grid points and the 1D models are compiled to obtain a 3D volume. This procedure has been described by *Shapiro and Ritzwoller* [2002], *Yang et al.* [2007b], and elsewhere.

Our specific approach to the second stage of inversion divides into two further steps. The first step is a linearized inversion of the dispersion curves for the 1D velocity structure at each grid point similar to the method of *Yang and Forsyth* [2006]. However, the best fitting model does not account for the non-uniqueness of the inverse problem; a variety of acceptable models may be created that fit the data within the estimated uncertainties. In the second step, for this reason, we perform a Monte-Carlo search of a corridor of model space defined by the results of the linearized inversion. From this we define an ensemble of velocity models that fit the data acceptably. These two steps are outlined further below. The linearized inversion procedure only uses Rayleigh and Love wave phase speed measurements while Rayleigh wave group speed measurements are also included in the Monte-Carlo procedure.

3.1. Starting Models, Parameterization, and Allowed Variations

Both the linearized inversion and the Monte-Carlo resampling of model space require a starting model. In the linearized inversion, we observe faster and more stable convergence by using unique starting models at each geographic point. For this purpose, we extract Vs values from the 3D model of *Shapiro and Ritzwoller* [2002]. The procedure also requires values of P-wave speed (Vp) and density (ρ). We use the average continental Vp/Vs ratios of 1.735 in the crust and 1.756 in the mantle from *Chulick and Mooney* [2002] who found little deviation from these values across the US. Furthermore, surface waves are less sensitive to Vp than Vs except in the uppermost crust. Density (ρ) is assigned similarly using a ρ/Vs ratio of 0.81 as described by *Christensen and Mooney* [1995]. Following previous work (e.g., *Weeraratne et al.* [2003]; *Yang and Forsyth* [2006]), we parameterize each model with 18 layers. Three crustal layers are used where the top layer thickness is set at the greater of 2 km or the sediment thickness from the model of *Laske and Masters* [1997]. The depth to the Moho was extracted from *Bassin et al.* [2000]. These two inputs define a thin upper crustal layer and a thick middle to lower crustal layer. The lower crustal layer was separated into two layers of equal thickness defining the middle and lower crust. The 15 layers in the mantle are between 20 and 50 km thick and extend to 410 km depth, but are relatively unconstrained by our data beneath 150 km. An illustration of the parameterization is shown in Figure 5a. In the linearized inversion, the velocities of all layers are allowed to change although regularization is applied to ensure smoothness, as discussed in Section 3.2 below. Vp/Vs and ρ/Vs are maintained at the values stated above. Finally, only the thicknesses of the lower crust and uppermost mantle are permitted to change. However, if poor data fit is observed, we perturb the upper and middle crustal layer thicknesses (while maintaining the initial crustal thickness) and the inversion is rerun.

For Monte-Carlo sampling we use the result of the linearized inversion as a starting model. However, we also impose an explicit requirement of monotonically increasing crustal velocity with depth. Within our study area, *Wilson et al.* [2003] and *Ozalaybey et al.* [1997] found evidence for a low-velocity zone (LVZ) in the crust from localized magma bodies and regional partial melt, respectively. Using receiver functions and surface wave dispersion to constrain the crust, *Ozalaybey et al.* [1997] allowed ∼20 crustal layers. At a variety of locations, their crustal LVZ was often 5 km or less in thickness. These crustal LVZs are of insufficient vertical extent for us to image reliably. Furthermore, a model parameterization using monotonically increasing isotropic crustal velocities still produces fairly good data fit in most cases. In the mantle, Monte-Carlo sampling of 15 mantle layers would be prohibitively expensive and would potentially create unrealistic models or require the additional complexity of a smoothing regularization. For speed and smoothness, we parameterize the mantle with five B-splines. An illustration of this parameterization of the model is shown in Figure 5b. *Ozalaybey et al.* [1997] found evidence for an upper mantle LVZ in northwestern Nevada, which is permitted in our mantle parameterization.

From the linearized inversion described above, we obtain smooth, simple 1D velocity profiles at all grid points which typically fit the data reasonably well. For the Monte-Carlo inversion, we define the allowed range of models based on this best fitting model. First, we impose a constraint on the permitted excursions from the initial velocity values. The velocity must be within $\pm$ 20% of the initial model in the upper crust and $\pm$ 10% in the lower crust and mantle. We choose this range rather than a specific velocity window (e.g., $\pm$ 0.5 km/s) because of the potential for unrealistically low values in the crust. By comparison, our allowed corridor is wider than that of *Shapiro and Ritzwoller* [2002]. Again, we maintain the Vp/Vs and Vs/ρ values stated above. However, the thicknesses of the crustal layers can now vary while the sum of crustal layers must be within $\pm$ 5 km of the Crust 2.0 model of *Bassin et al.* [2000]. The Q model from PREM (*Dziewonski and Anderson* [1981]) is used for the physical dispersion correction, and all models are reduced to 1 sec period.

Complexities probably exist within the crust and upper mantle that may not be well represented by our simple parameterization. However, if data fit is within uncertainties in the dispersion maps, we cannot empirically justify a more complicated model without inclusion of independent information (e.g., receiver functions), which is beyond the scope of this study.

3.2. Linearized Inversion

The linearized inversion process uses the starting model described in section 3.1 to create predicted dispersion curves. Perturbing the input model provides misfit information and iterating converges upon the best-fitting model. The linearized inversion process follows the work of *Li et al.* [2003], *Weeraratne et al.* [2003], *Forsyth and Li* [2005], *Yang and Forsyth* [2006] and others. In this case, the forward code used to compute dispersion curves from an input model is based on *Saito* [1988]. Only Rayleigh and Love wave phase speed curves are used in the inversion. Rayleigh wave group speed curves are introduced in the Monte-Carlo inversion, however.

The technique to find the best fitting velocity model is outlined by *Weeraratne et al.* [2003] and is based on the iterative least-squares approach of *Tarantola and Valette* [1982]. *Li et al.* [2003] concisely summarize the approach, which we excerpt here. The solution is described by the equation:

$$\mathbf{\Delta m} = (\mathbf{G}^T\mathbf{C}_{nn}^{-1}\mathbf{G} + \mathbf{C}_{mm}^{-1})^{-1}(\mathbf{G}^T\mathbf{C}_{nn}^{-1}\mathbf{\Delta d} - \mathbf{C}_{mm}^{-1}[\mathbf{m} - \mathbf{m_0}]) \tag{1}$$

where $\mathbf{m}$ is the current model, $\mathbf{m_0}$ is the starting model at the outset of each iteration, and $\mathbf{\Delta m}$ is the change to the model. $\mathbf{\Delta d}$ is the difference between the observed and predicted data. $\mathbf{G}$ is a sensitivity matrix relating changes in $\mathbf{d}$ to changes in $\mathbf{m}$. $\mathbf{C}_{mm}$ is the model covariance matrix where non-zero values (we use 0.l) are introduced into the off-diagonal terms in order to provide a degree of correlation between velocity values obtained for adjacent layers and ensure a reasonable model (i.e., a model without large velocity jumps or oscillations). $\mathbf{C}_{nn}$ is the diagonal data covariance matrix where the diagonal elements are calculated from the local uncertainties in the dispersion maps.

As a measure of data fit, we use reduced χ^2 (henceforth χ^2). Unique χ^2 values are computed for Rayleigh wave and Love wave phase speed; χ^2 is also computed for Rayleigh wave group speed in the Monte-Carlo resampling described below. χ^2 is defined as

$$\chi^2 = \frac{1}{n}\sum_{i=1}^{n}\frac{(\tilde{d}_i - d_i)^2}{\sigma_i^2} \qquad (2)$$

where i is the index of the period of the measurement through all wave types used. Periods used are on a 2 second grid from 8 - 20 s period and every 5 seconds for 25 - 70 s period. Therefore, n is 7 for Love waves and 17 for Rayleigh waves. Thus, in the linearized inversion, 24 measurements are used but in the Monte-Carlo inversion, 41 measurements are applied because Rayleigh wave group speeds are utilized. $\tilde{d}$ and d_i are the model predicted and measured wave speeds, respectively, and σ_i is the uncertainty of the measured velocity unique to each period, wave type, and location, as described in Section 2 above. A χ^2 value of 2 or less represents fairly good data fit, although misfit systematics may still exist for χ^2 ranging from 1.5 to 2. Higher values indicate inferior fit, inadequate model parameterization, or underestimated data uncertainties.

An example of input data and model output from the linearized inversion is shown in Figure 6 for a point in Illinois. For reference, the location of this point is plotted as a grey circle in Figure 1. Dispersion observations and associated errors are plotted as error bars in Figure 6a. The resulting best fitting model and related dispersion curves produced by linearized inversion are shown as thin black lines. For comparison, the starting model and the related dispersion curves are shown in Figure 6 as dotted grey lines.

Variability in data fit is present in the study area. Figure 7 shows two more examples like Figure 6 but with higher resulting χ^2 values. Considering that the location of data used in Figure 7c,d is in an area of particularly good resolution (southern California), the misfit most likely derives from improper model parameterization. In this case, the short period under-prediction of Love wave speeds and over-prediction of Rayleigh wave speeds may indicate the need for radial anisotropy in the crust. More discussion of alternative parameterizations follows in Section 6.3. Examination of the sensitivity curves in Figure 3 suggests that higher misfit (e.g., Figure 7a,c) could be due to improper model parameterization at depths from 0 - 30 km.

3.3. Monte-Carlo Resampling and Model Uncertainty Estimation

To estimate uncertainties in geophysical inverse problems, model space sampling methods such as Monte-Carlo methods have been in use for over 40 years (*Keilis-Borok and Yanovskaya* [1967]) and can provide useful uncertainty estimates even when the *a priori* probability density of solutions is unknown (see *Mosegaard and Tarantola* [1995]). Variations among Monte-Carlo methods are summarized by *Sambridge and Mosegaard* [2002]. One particular concern in our inverse problem is the tradeoff between velocity values in the lower crust and uppermost mantle with crustal thickness. This is considered a significant problem by *Marone and Romanowicz* [2007] and elsewhere and provides part of our motivation to estimate model uncertainty. We quantify the variation of acceptable models and use this variation as an indication of the robustness of the resulting velocity model. Nevertheless, as discussed in section 2, because the estimates of the uncertainty of the dispersion maps are subjective, the estimates of model uncertainty are also.

The Monte-Carlo procedure is a two-step process that first creates models through uniformly distributed random perturbations within the permitted corridor around the model produced by linearized inversion. Second, a random walk is used to refine the search for acceptable models. Rayleigh wave group and phase and Love wave phase speed dispersion curves are generated for each model using the faster forward code of *Herrmann* [1987] which we verified agrees well with the code of *Saito* [1988] used in the linearized inversion. If the predicted dispersion curves match the measured results at an acceptable level, the model is retained. An acceptable model is defined as one having a χ^2 value within 3 times the χ^2 value obtained from the linearized inversion. Fairly conservative error estimates result from these choices. In order to accelerate the process of obtaining a sufficient number of acceptable models, the random walk procedure generates small perturbations to search adjacent model space for additional acceptable models. After the random walk identifies an acceptable model, the search re-initializes in the neighborhood of that model until we construct 100 acceptable models. This number of models is arbitrary, but appears to be large enough to quantify model uncertainty to form the basis for our inferences and is computationally tractable. An example of the observed dispersion curves and the Monte-Carlo results are shown in Figure 8 for points labeled as grey squares in Figure 1.

We select a "favored model" from the set of resulting velocity models. The best-fitting model is very similar to that determined through linearized inversion and may not represent the ensemble of models very well. We favor the model closest to the mean of the distribution, where greater depths are given lesser weight. This captures the essence of the ensemble but diminishes the occasional problems of lateral roughness found when only the best fitting velocity models are considered. For illustration, the models identified as most near the mean of the distribution are plotted in red in Figure 8a,c,e and are, henceforth, referred to as the "favored models". Further discussion of model variability across the study area is reserved for Section 5 below.

4. Crustal Rayleigh/Love Wave Speed Discrepancy

The observation of relatively poor data fit in regions of good resolution deserves further comment. A three-layer crust and multi-layer mantle can usually fit either Rayleigh or Love wave measurements satisfactorily. However, fitting data to both simultaneously is more difficult. Figure 9 shows the difference in misfit to Rayleigh and Love waves phase velocities across the US where, unlike χ^2, the sign of the misfit is retained. The predicted curves are from the "favored model" derived by Monte-Carlo inversion from which we subtract the observed dispersion at each geographical point and divide this by the estimated data error. These values are averaged only from 8 - 20 s period. Green and orange colors signify that the model is faster than an observation at a point. Blue colors indicate that the model is too slow to fit the observations. The widespread result of Rayleigh and Love wave speeds being over- and under-predicted, respectively, is apparent. The period band (8 - 20 s) indicates that the source of this discrepancy lies in the crust. We, therefore, refer to this as the crustal Rayleigh/Love discrepancy to distinguish it from the well known mantle Rayleigh/Love discrepancy caused by radial anisotropy due to olivine alignment in the mantle (e.g., *Dziewonski and Anderson* [1981]). Section 6.3 below discusses possible causes of this observation and the preferred explanation.

5. Results

We construct a "favored model" from an ensemble of models that fit the data acceptably developed through Monte-Carlo inversion at each grid point. Combining these 1D isotropic models, we obtain a 3D shear wave velocity model for the continental US with lateral coverage bounded approximately by the black contour in Figure 2 and depth range from the surface to 150 km. Here, we characterize the model by highlighting examples of the types of features it contains. The names of features listed in Figure 2.

Because the model is over-parameterized, we smooth the model features and soften abrupt contrasts between layers by vertically averaging in 4 km increments in the crust and 10 km in the mantle. Thus, a depth section at 10 km is the average from 8 - 12 km depth. No smoothing is applied across the Moho. In addition, we average model values from four horizontally adjacent grid nodes (across 1 degree) so that map views represent a 1 degree average of the original model values. Tests indicate that such smoothing does not degrade data fit substantially. However, the lateral smoothing does reduce vertical striping on plots of vertical cross-sections.

5.1. Characteristics of the 3D Model

Horizontal slices of isotropic shear wave speed at a selection of depths are shown in Figure 10 including 4 km above (Figure 10c) and 4 km below (Figure 10d) the estimated Moho depth. The most striking features at 4 km depth (Figure 10a) are several large sedimentary basins. The Mississippi Embayment and the Green River Basin appear most strongly. Additionally, the Williston Basin and Anadarko Basin in Montana and Oklahoma, respectively, clearly appear as slow velocity anomalies. Low velocities associated with the sediments of the Great Valley in California abut slow crustal velocities of the Cenozoic Pacific Northwest volcanic province farther north. A trend of generally faster velocities in the eastern US compared with the western US is also seen. This is observed at all depths and we refer to it as the east-west crustal "dichotomy" in the US. At 10 km (Figure 10b), the most pronounced feature is again the deep sediments of the Mississippi Embayment, which may be partially extended to this depth by the vertical averaging.

The crustal velocity dichotomy at this depth is located along the boundary between the Great Plains and Central Lowlands as will be discussed further in Section 6.2 below.

In the lower crust at 4 km above the Moho, Figure 10c shows that the crustal velocity dichotomy in the central US shifts west to coincide with the transition from the Great Plains to the Rocky Mountain Front. The slow anomaly in the Basin and Range may be attributed to high crustal temperatures in this extensional province, as evidenced by high surface heat flow in the area (see e.g., *Blackwell et al.* [1990]). The fast anomaly in Michigan may result from regionally thicker crust; a slice at 4 km above the Moho is at a greater depth than the surrounding region. However, the slower speeds beneath the Appalachian Highlands to the east is within similarly thick crust, implying that compositional differences between the Appalachian Highlands and the continental shield are the more likely cause of this velocity anomaly. For reference, the estimated crustal thickness is shown in Figure 11.

In the upper mantle 4 km below the Moho (Figure 10d), the east-west velocity dichotomy is in a similar but not identical location to the lower crust. This will be discussed further in Section 6.2 below. East of this transition, more laterally homogeneous mantle velocities appear. To the west, the prominent slow anomaly below the eastern Basin and Range corroborates the suggested removal of mantle lithosphere from 10 Ma to present (e.g., *Jones et al.* [1994]) and replacement with warmer, low velocity asthenospheric material. The slow anomaly in the Pacific Northwest can be attributed to the volatilized mantle wedge residing above the subducting slab. At 80 km depth (Figure 10e), however, the slow anomaly associated with the mantle wedge is no longer visible, suggesting that this depth is below or within the subducting slab. Also, a slow mantle velocity anomaly extends in the northwest to southeast direction, roughly following the outline of the entire Basin and Range province. A similar feature was also observed in the tomographic models of *Alsina et al.* [1996] and others and has been attributed to inflow of warm mantle material during Cenozoic extension (e.g., *Wernicke et al.* [1988]). At 120 km depth in Figure 10f, features are similar to 80 km depth, but anomalies are of lower amplitude.

The estimated crustal thickness is similar to the starting model of Crust 2.0 (*Bassin et al.* [2000]) and is shown in Figure 11. On average, the crust is 1.6 km thinner than Crust 2.0 and the RMS difference from Crust 2.0 across the study region is 1.5 km. The relation of crustal thickness with topography and implications for topographic support or compensation are discussed in section 6.1.

Figure 12 presents a series of vertical cross-sections with locations indicated on the map in Figure 12a. A smoothed elevation profile is plotted above each cross-section and a profile of the recovered crustal thickness is overplotted. We use different color scales for crustal and mantle shear wave speeds. The vertical exaggeration of the cross-sections is roughly 25:1 and the same horizontal scale is used for N-S and E-W cross-sections.

As with the horizontal depth-sections presented in Figure 10, the most pronounced shallow crustal velocity anomalies are from sedimentary basins, although vertical smoothing extends these features to greater depths. Profiles C-C' and F-F', for example, show that the sediments of the Mississippi Embayment extend inland from the coast for hundreds of kilometers. The most pronounced velocity contrasts result from the location of the east-west velocity dichotomy in the crust and upper mantle, as discussed further in Section 6.2. Slow mantle velocities extend from the Rocky Mountains to the west and are particularly low in the Basin and Range.

5.2. Model Uncertainties

As discussed in section 3.3, a model is considered to be a member of the ensemble of acceptable models if its χ^2 misfit is within three times that of the best fitting model from the linearized inversion. The standard deviation (σ, not to be confused with measurement uncertainty) of this ensemble at each grid point then defines the confidence in the velocity values through depth and across the study region. Average values for σ versus depth are shown in Figure 13a. Except near the surface, the average value of uncertainty is about 1.5%, with this value increasing slightly with depth. The RMS of velocities as a function of depth taken over the entire region of study is also shown in Figure 13 to be about 3%, except near the surface. Thus, lateral velocity anomalies are, on average, about twice the size of the uncertainties.

Figure 14 shows the amplitude and distribution of σ across the study region at the depths presented in Figure 10. At 4 km depth, σ is greatest near the edges of the study area, in part due to higher expected data errors caused by lower resolution. Low σ values at 10 km depth (Figure 14b) through much of the study region are due to the lack of boundaries above and below this layer with which to trade-off. A parameterization that allows topography on more crustal layers would generate greater middle crustal uncertainty. In the lower crust (Figure 14c), σ is greater than in the mid-crust due to the tradeoff between wave speed and crustal thickness. Similar values are observed in the upper mantle (Figure 14d) due to the same tradeoff. At 80 km (Figure 14e), σ is lower than at shallower depths and is more uniform. The uniformity extends to about 120 km depth (Figure 14f), although the amplitude of σ increases slightly at this depth due to poorer sensitivity at greater depths as indicated in Figure 3. Below 150 km depth, the model is very poorly constrained.

Figure 13b shows the average standard deviation in the dispersion curves produced by the ensemble of acceptable models. Greater variability in model velocity values in the uppermost crustal layer results in the higher standard deviation values at short periods (i.e., < 15 s period). Rayleigh and Love wave phase speed variability is nearly constant at 0.5% while the Rayleigh wave group speed variability is higher due to the higher.

6. Discussion

A detailed interpretation of the estimated 3D model is beyond the scope of this paper. We discuss three specific questions and emphasize using the model uncertainties to address them. First, we consider the relation between crustal thickness and surface topography across the US. Second, we constrain the location of the east/west velocity dichotomy in the lower crust and uppermost mantle. Finaly, we present alternative model parameterizations in the attempt to illuminate the cause of the crustal Rayleigh/Love velocity discrepancy discussed in Section 4 above.

6.1. Topographic Compensation

The relation between surface topography, crustal thickness, and crust and mantle velocities allows qualitative conclusions to be drawn regarding the support for high topography in the US. In general, surface topography within the US is not well correlated with crustal thickness. For example, the north-south profiles in Figure 10 display very little relation between the surface and Moho topography. Profile E-E', in particular, reveals crustal thickness to be anti-correlated with topography and substantial Moho topography exists under regions with almost no surface topography in Profiles F-F' and G-G'. In addition, the Basin and Range province is characterized by high elevations, but the crust is relatively thin. In all of these areas, however, high elevations with relatively thin crust are underlain by a slower and presumably less dense crust and mantle, indicative of a Pratt-type of compensation or dynamical support for the topography. There are exceptions, however. Running from west to east along Profile B-B', the highest elevations coincide with a mantle that is relatively slow and the crust is thick. Farther east in the Great Plains, the thinning crust and decreasing elevation are coincident, suggesting an Airy-type of compensation.

6.2. East-West Shear Velocity Dichotomy

The difference in crustal and uppermost mantle shear wave speeds between the faster tectonically stable eastern US and the slower tectonically active western US is visible in the horizontal and vertical cross-sections presented in Figures 10 and 12. This is also a feature of older tomographic models. Here, we use the ensemble of models from the Monte-Carlo inversion to estimate the location of and uncertainty in this velocity dichotomy.

First, Figure 15 presents histograms of velocity values along 40°N within the eastern and western US for the lower crust and in the mantle at 80 km depth. The values are taken from the favored model produce by the Monte Carlo inversion. The eastern and western US are separated approximately by a shear velocity of about 3.75 km/sec in the lower crust and 4.55 km/sec in the uppermost mantle, but the exact choice of these values affects our conclusions only slightly. Note first that the two distributions are nearly disjoint, indicating a strong compositional and/or thermal difference between the tectonically active western US and the stable eastern US. Secondly, the distribution in the eastern US is more peaked, particularly in the lower crust, demonstrating that the eastern US is somewhat more homogeneous than the west.

To estimate the location of the boundary of the east-west dichotomy, shear velocity values for the lower crust and at 80 km depth are sorted and ranked by V_s value for the ensemble of 100 acceptable models produced by the Monte Carlo inversion at each grid point. In Figure 16, contours are plotted through the 20th and 80th maps (which can be thought of as the 20th and 80th percentile values within the ensemble of accepted models at each point) for values of 3.75 km/s in the lower crust and 4.55 km/s at 80 km depth as grey and black lines, respectively. The separation between the tectonically active western US and the stable eastern US lies approximately between these contours. In the lower crust (Figure 16a), the western velocity contrast roughly follows the Rocky Mountain Front from Wyoming to the south, but veers to the west north of central Wyoming, crossing the Rocky Mountain front. This east-west contrast occurs abruptly. In fact, examining the lower crustal velocity values across a variety of latitudes, a velocity change of roughly 300 m/s typically occurs over less than 100 km laterally. Both the 20th and 80th percentile values are seen in the western US. In the eastern US, the 20th percentile contour outlines the southeastern edge between the North American craton and the Appalachian Highlands farther east. This velocity contour does not precisely follow the western edge of the Appalachian highlands as plotted in Figure 2, which may be due to the lower resolution in the eastern US. The Mid-Continental Rift (MCR), oriented in a NNE-SSW direction in the central US, is also apparent. This feature is subtle in velocity depth- and cross-sections but clearly appears here, with a location that agrees with the configuration apparent in gravity maps.

At 80 km depth in the mantle, a similar set of contours outlines the eastern edge of the slower western US. However, the location of these contours now aligns better with the Rocky Mountain Front in the northern part of the study area and lies farther east in the southern portions. The eastern contour provides an outline of the cratonic lithosphere.

In summary, the range of locations is sufficiently narrow to constrain the boundary of the dichotomy in the lower crust and uppermost mantle and to observe that these locations are similar but not identical. First, the fact that slower and presumably less dense mantle material often extends well east of the Rocky Mountain Front suggests that mantle compensation plays a role in the high topography of that region. Second, the dichotomy boundary in the lower crust lies west of the mantle boundary in the western US. Assuming that this boundary marks the approximate edge of the craton, this means that the cratonic crust extends out farther from the interior of the craton than the cratonic mantle. This apparent overhanging of the cratonic crust may be caused by mantle lithospheric erosion due to small-scale convection. Third, the lower crustal boundary crosses the Rocky Mountain front, probably reflective of crustal deformation beneath and west of the northern Rocky Mountains.

6.3. Resolving the Crustal Rayleigh/Love Wave Speed Discrepancy

Section 4 documents the systematic misfit of Rayleigh and Love wave phase velocities below about 20 sec period by a simple isotropic parameterization of the crust with monotonically increasing velocities with depth. Figure 9 presents a summary that shows that, on average, Rayleigh wave speeds are overpredicted and Love wave speeds are underpredicted by the isotropic model that aims to fit both simultaneously. Figure 17a shows an example inversion for a point in northwest Utah (located with a grey star in Figure

1) illuminating how the estimated isotropic model (red line) predicts Love wave speeds that are too slow and Rayleigh wave speeds that are too fast, particularly below about 15 sec period. Apparently, the model parameterization is inadequate to fit both types of data simultaneously. The most likely cause of the problem is either the constraint that imposes vertical monotonicity within the crust or the fact that only isotropic models are constructed within the crust. We test both alternatives.

To determine whether crustal radial anisotropy can resolve the short period Rayleigh-Love discrepancy, we allow only the middle crust to be radially anisotropic. The rest of the model is fixed on the favored model from the isotropic profiles determined from the Monte-Carlo inversion. We perform a grid search over small perturbations in Vs in the middle crust ($\pm$500 m/s) which attempts to fit the Rayleigh and Love wave phase velocity measurements below 25 sec separately. In the inversion with the Rayleigh wave data alone we recover a set of allowed Vsv values in the middle crust and with the Love wave data we get a set of allowed Vsh values. The model is isotropic outside the middle crust. The result for the best fitting radially anisotropic model for the point in northwest Utah is shown in Figure 17a (blue line). The model itself with bifurcated Vsh and Vsv values is shown in Figure 17b where blues denote Vsv and reds denote Vsh in the middle crust and the model outside the middle crust is isotropic ($Vsh = Vsv = V_s$). In general, allowing radial anisotropy in the middle crust can resolve the Rayleigh - Love discrepancy. We have also performed the experiment allowing lower crustal radial anisotropy, but on average it does not fit the data as well as middle crustal anisotropy alone. A combination of middle and lower crustal radial anisotropy cannot be ruled out, however.

Although Love waves are predominantly sensitive to Vsh and Rayleigh waves to Vsv, there is weak sensitivity of each wave type to the alternate shear wave speed. Thus, separately inverting Love and Rayleigh waves for Vsh and Vsv, respectively, is not fully accurate. To test the approximation, we performed tests using the anisotropic "MINEOS" code of *Masters et al.* [2007]. We created synthetic dispersion curves from models possessing radial anisotropy in the crust and then inverted them to estimate the anisotropy using the procedure outlined above. The approximation we apply recovers the initial model to within about 5 m/s (~0.1%), which is an order of magnitude smaller than the amplitude of the dispersion signals that are attempting to explain. The approximation that we use, therefore, is sufficiently accurate for the inferences drawn here.

We have also investigated whether breaking the monotonicity constraint can resolve the Rayleigh - Love discrepancy. An example inversion in which a fourth crustal layer has been introduced and the monotonicity constraint has been broken is shown with the green lines in Figure 17. In this case a low velocity zone (LVZ) is introduced in the lower crust. Breaking the monotonicity constraint and introducing another crustal layer improves the fit to the data, but does not resolve the discrepancy as well as allowing a single middle crustal anisotropic layer. We extended this test across all of Nevada where radial anisotropy improves data fit and where crustal low velocity zones have been previously documented. *Ozalaybey et al.* [1997] found thin crustal LVZs (~5 km thick) at points in this area using a joint receiver function/surface wave technique. For the 93 grid points tested, our procedure was not able to obtain the quality of fit observed using radial anisotropy, as the misfit results in Table 1 show. The values contained within the table are averaged over dispersion measurements from 10 to 20 sec period. We find that the χ^2

misfit with the radially anisotropic crust across Nevada is 1.06, yielding $\sim 42\%$ variance reduction compared to the isotropic model with monotonically increasing shear wave speeds. The non-monotonic isotropic model gives only a 15% variance reduction, with a χ^2 value of 1.54, and misfit systematics continue in evidence. Breaking the monotonicity constraint and adding a single crustal layer, therefore, does not allow the data to be as fit well as by allowing radial anisotropy in a single crustal layer. The introduction of more crustal layers and the development of more complicated models cannot be formally ruled out as an alternative, but the layerization will have to be extensive and complicated.

Thus, the introduction of radial anisotropy to the model parameterization is most effective at resolving the discrepancy and we believe radial anisotropy is the most likely physical cause. The mapping of radial anisotropy in the upper mantle using fundamental mode Rayleigh and Love waves is a well established technique (e.g., *Tanimoto and Anderson* [1984], *Montagner* [1991]). *Shapiro et al.* [2004] used longer period Rayleigh and Love wave observations to constrain radial anisotropy in the Tibetan crust, which they attributed to crystal alignment caused by crustal flow. The widespread search for crustal radial anisotropy has been hindered by a lack of short period dispersion observations (below 20 sec period) over extended regions, which ambient noise tomography now provides.

Figure 18a presents the middle crustal radial anisotropy for the best fitting radially anisotropic model, where green and orange colors indicate positive anisotropy ($Vsh > Vsv$) and blue colors indicate the reverse. In this compilation, most of the US has crustal radial anisotropy above the level of $\pm 1\%$ and most areas have positive anisotropy. This does not mean, however, that the anisotropy is required to fit the data. To determine this we present in Figure 18b the model with the minimal anisotropy that fits the data acceptably. In this result, the middle crust across much of the US is white (i.e., isotropic) and the regions with negative anisotropy largely disappear.

There remain in Figure 18b several regions in which radial anisotropy in the middle crust is required to fit the data. These regions tend to be of two main tectonic types: sedimentary basins and extensional regions. The Anadarko (western Oklahoma), Appalachian, and Green River (western Wyoming) basins are clearly outlined. In these cases, layering of sediments may cause different *Vsh* and *Vsv* values in the uppermost crust and some improvement in data fit is observed by allowing radial anisotropy in the middle crust. These features may be artifacts, however, caused by poor parameterization of the vertical V_s velocity gradient in the sediments or perhaps by the strong lateral contrast across which the Love and Rayleigh waves sample differently (e.g., *Levshin and Ratnikova* [1984]). Crustal radial anisotropy at about 2 - 4 % is observed through much of the Basin and Range, extending southeast toward the Rio Grande Rift. The observed radial anisotropy may be due to crystalline reorganization effected during Cenozoic extension. *Shapiro et al.* [2004] attributed observed radial anisotropy to the alignment of mica crystals in the crust. The effects of other compositional organizations, such as aligned cracks (e.g., *Crampin and Peacock* [2005]) or layering (e.g., *Crampin* [1970]), have also been shown to cause seismic anisotropy. The multiplicity of sources of radial anisotropy must be considered when interpreting these results.

Presentation of the 3D distribution of *Vsh* and *Vsv* and further investigation of alternative parameterizations and physical causes await more exhaustive studies based on the USArray/Transportable Array.

7. Conclusions

We present a 3D shear velocity model of the crust and uppermost mantle beneath much of the continental United States. The model is constrained by Rayleigh group and phase velocity measurements from 8 to 70 s period and Love wave phase velocities from 8 to 20 s, both determined by ambient noise tomography (ANT) presented previously by *Bensen et al.* [2008]. We employ a two-step procedure to obtain shear wave speeds in the crust and uppermost mantle from the surface to approximately 150 km depth. In the first step, a linearized inversion is performed to find the best fitting model at each grid point on a 0.5° x 0.5° grid across the US. This is followed in the second step by a Monte-Carlo inversion to estimate the ensemble of models that fit the data acceptably and, hence, to bound model uncertainties.

The 3D model presented here displays higher lateral resolution than earlier models produced using teleseismic earthquake data on a similar scale. Unexpectedly, the amplitude of features in the model, however, tend to be muted relative to global models such as that of *Shapiro and Ritzwoller* [2002]. At the largest scales, the outline of the structural dichotomy between the tectonic west and the stable eastern part of the US is clearly defined in both the crust and uppermost mantle and is observed to be very abrupt. The location of the transition between the tectonic and stable regions is shown to be similar in the lower crust and uppermost mantle, but not coincident. In the western US, high velocities in the crust typically extend further to the west than in the mantle, particularly north of Colorado. On smaller scales, numerous intriguing features within the model are imaged, such as sedimentary basins in the shallow crust, the indication of the mid-continental rift in the lower crust, and the generally variable correlation between surface and Moho topography across much of the country. The estimated crustal thickness is similar to model Crust 2.0 of *Bassin et al.* [2000] across most of the US.

The resulting isotropic 3D model systematically misfits Rayleigh and Love wave speeds between 10 and 20 sec period in some regions, overpredicting Rayleigh wave speeds and underpredicting Love wave speeds. We argue that this Rayleigh/Love discrepancy probably results from radial anisotropy in the middle and/or lower crust. Crustal radial anisotropy is required primarily within the Basin and Range and other extensional provinces, with $Vsh > Vsv$ by about $\sim$1% in these regions. A more exhaustive study of the Rayleigh/Love discrepancy using alternative model parameterizations, higher resolution data (e.g., from the USArray Transportable Array), and other kinds of data (e.g., receiver functions) is a natural extension of this work.

8. Acknowledgements

The authors are deeply grateful to Goran Ekstrom, an anonymous referee and the anonymous Editor for exceptionally conscientious and detalied comments that helped to improve this paper. All of the data used in this research were downloaded either from the IRIS Data Management Center or the Canadian National Data Center (CNDC). This research was partially supported by a contract from the US Department of Energy, DE-FC52-2005NA26607, and two grants from the US National Science Foundation, EAR-0450082 and EAR-0711526. We are grateful for the support of Chuck Meertens throughout this project and the GEON project support for GDB (EAR-0408228).

References

Alsina, D., R. L. Woodward, and R. K. Snieder (1996), Shear wave velocity structure in North America from large-scale waveform inversions of surface waves, *J. Geophys. Res.*, *101*(B7), 15,969–15,986.

Barmin, M. P., M. H. Ritzwoller, and A. L. Levshin (2001), A fast and reliable method for surface wave tomography, *Pure Appl. Geophys.*, *158*(8), 1351–1375.

Bassin, C., G. Laske, and G. Masters (2000), The current limits of resolution for surface wave tomography in North America, *EOS Trans. AGU*, *81*, F897.

Bensen, G. D., M. H. Ritzwoller, M. P. Barmin, A. L. Levshin, F. Lin, M. P. Moschetti, N. M. Shapiro, and Y. Yang (2007a), Processing seismic ambient noise data to obtain reliable broad-band surface wave dispersion measurements, *Geophys. J. Int.*, *169*, 1239–1260.

Bensen, G. D., M. H. Ritzwoller, and N. M. Shapiro (2008), Broad-band ambient noise surface wave tomography across the United States, *J. Geophys. Res., 113*, B05306, doi:10.1029/2007JB005248.

Blackwell, D., J. Steele, and L. Carter (1990), Heat flow patterns of the North American continent: A discussion of the DNAG Geothermal Map of North America.

Christensen, N. I., and W. D. Mooney (1995), Seismic velocity structure and composition of the continental crust: A global view, *J. Geophys. Res.*, *100*(B6), 9761–9788.

Chulick, G. S., and W. D. Mooney (2002), Seismic structure of the crust and uppermost mantle of North America and adjacent oceanic basins: A synthesis, *Bull. Seis. Soc. Am.*, *92*(6), 2478–2492.

Crampin, S. (1970), The dispersion of surface waves in multilayered anisotropic media, *Geophys. J. Astr. Soc.*, *21*, 387–402.

Crampin, S., and S. Peacock (2005), A review of shear-wave splitting in the compliant crack-critical anisotropic Earth, *Wave Motion*, *41*(1), 59–77.

Crotwell, H. P., and T. J. Owens (2005), Automated receiver function processing, *Seis. Res. Lett.*, *76*(6), 702–709.

Dziewonski, A. M., and D. L. Anderson (1981), Preliminary reference Earth model, *Phys. Earth Plan. Int.*, *25*(4), 297–356.

Ekström, G., J. Tromp, and E. W. F. Larson (1997), Measurements and global models of surface wave propagation, *J. Geophys. Res.*, *102*(B4), 8137–8157.

Forsyth, D. W., and A. Li (2005), Array-analysis of Two-dimensional Variations in Surface Wave Phase Velocity and Azimuthal Anisotropy in the Presence of Multipathing Interference, *Seismic Earth: Array Analysis of Broadband Seismograms*, pp. 81–98.

Gao, W., S. P. Grand, W. S. Baldridge, D. Wilson, M. West, J. F. Ni, and R. Aster (2004), Upper mantle convection beneath the central Rio Grande Rift imaged by P and S wave tomography, *J. Geophys. Res.*, *109*(B03), 3305–3305.

Godey, S., R. K. Snieder, A. Villaseñor, and H. M. Benz (2003), Surface wave tomography of North America and the Caribbean using global and regional broad-band networks: phase velocity maps and limitations of ray theory, *Geophys. J. Int.*, *152*(3), 620–632.

Grand, S. P. (1994), Mantle shear structure beneath the Americas and surrounding oceans, *J. Geophys. Res.*, *99*(B6), 11,591–11,622.

Grand, S. P. (2002), Mantle shear-wave tomography and the fate of subducted slabs, *Philosophical Transactions: Mathematical, Physical and Engineering Sciences*, *360*(1800), 2475–2491.

Herrmann, R. B. (1987), Computer programs in seismology, *St. Louis University, St. Louis, Missouri.*

Jones, C. H., H. Kanamori, and S. W. . Roecker (1994), Missing roots and mantle “drips”: Regional Pn and teleseismic arrival times in the southern Sierra Nevada and vicinity, California, *J. Geophys. Res.*, *99*(B3), 4567–4601.

Karlstrom, K. E., et al. (2002), CD-ROM working group. 2002. Structure and evolution of the lithosphere beneath the Rocky Mountains: initial results from the CD-ROM experiment, *GSA Today*, *12*(3), 4–10.

Keilis-Borok, V. I., and T. B. Yanovskaya (1967), Inverse problems in seismology (structural review), *Geophys. J. Astr. Soc.*, *13*, 223–234.

Kennett, B. L. N., E. R. Engdahl, and R. Buland (1995), Constraints on seismic velocities in the Earth from traveltimes, *Geophys. J. Int*, *122*(1), 108–124.

Laske, G., and G. Masters (1997), A global digital map of sediment thickness, *EOS Trans. AGU*, *78*, 483.

Lee, W. B., and S. C. Solomon (1978), Simultaneous inversion of surface wave phase velocity and attenuation: Love waves in western North America, *J. Geophys. Res.*, *83*(B7), 3389–3400.

Levshin, A., and L. Ratnikova (1984), Apparent anisotropy in inhomogeneous media, *J. Astron. Soc.*, *76*(1), 65–69.

Levshin, A. L., V. F. Pisarenko, and G. A. Pogrebinsky (1972), On a frequency-time analysis of oscillations, *Ann. Geophys.*, *28*(2), 211–218.

Li, A., D. W. Forsyth, and K. M. Fischer (2003), Shear velocity structure and azimuthal anisotropy beneath eastern North America from Rayleigh wave inversion, *J. Geophys. Res.*, *108*(10.1029).

Lin, F., M. P. Moschetti, and M. H. Ritzwoller (2007), Surface wave tomography of the western United States from ambient seismic noise: Rayleigh and Love wave phase velocity maps, *Geophys. J. Int.*, submitted.

Lin, F., M. H. Ritzwoller, and R. Snieder (2009), Eikonal Tomography: Surface wave tomography by phase-front tracking across a regional broad-band seismic array, *Geophys. J. Int.*, submitted.

Marone, F., and B. Romanowicz (2007), Non-linear crustal corrections in high-resolution regional waveform seismic tomography, *Geophys. J. Int.*, *170*(1), 460–467.

Marone, F., Y. Gung, and B. Romanowicz (2007), Three-dimensional radial anisotropic structure of the North American upper mantle from inversion of surface waveform data, *Geophys. J. Int.*, *171*(1), 206–222, doi:10.1111/j.1365-246X.2007.03465.x.

Masters, G., M. P. Barmine, and S. Kientz (2007), MINEOS user manual version 1.0, *Computational Infrastructure for Geodynamics*, http://www.geodynamics.org/cig/software/packages/seismo/mineos/ .

Montagner, J. P. (1991), Global upper mantle tomography of seismic velocities and anisotropies, *J. Geophys. Res.*, *96*(B12), 20,337–20,351.

Moschetti, M. P., M. H. Ritzwoller, and N. M. Shapiro (2007), Surface wave tomography of the western United States from ambient seismic noise: Rayleigh wave group velocity maps, *Geochem. Geophys. Geosys.*, *8*(Q08010), doi:10.1029/2007GC001655.

Mosegaard, K., and A. Tarantola (1995), Monte Carlo sampling of solutions to inverse problems, *J. Geophys. Res.*, *100*(B7), 12,431–12,448.

Nettles, M., and A. M. Dziewonski (2008), Radially anisotropic shear velocity structure of the upper mantle globally and beneath North America, *J. Geophys. Res.*, *113*(B02303), doi:10.1029/2006JB004819.

Nolet, G. (1990), Partitioned waveform inversion and two-dimensional structure under the network of autonomously recording seismographs, *J. Geophys. Res.*, *95*(B6), 8499–8512.

Ozalaybey, S., M. K. Savage, A. F. Sheehan, J. N. Louie, and J. N. Brune (1997), Shear-wave velocity structure in the northern Basin and Range province from the combined analysis of receiver functions and surface waves, *Bull. Seis. Soc. Am.*, *87*(1), 183–199.

Ramachandran, K., S. E. Dosso, G. D. Spence, R. D. Hyndman, and T. M. Brocher (2005), Forearc structure beneath southwestern British Columbia: A three-dimensional tomographic velocity model, *J. Geophys. Res.*, *110*(B2), 2303(17), doi: 10.1029/2004JB003258.

Ritzwoller, M. H., and A. L. Levshin (1998), Eurasian surface wave tomography - group velocities, *J. Geophys. Res.*, *103*(B3), 4839–4878.

Ritzwoller, M. H., N. M. Shapiro, M. P. Barmin, and A. L. Levshin (2002), Global surface wave diffraction tomography, *J. Geophys. Res.*, *107*(B12), 2335–2347, doi: 10.1029/2002JB001777.

Saito, M. (1988), DISPER80: A subroutine package for the calculation of seismic normal-mode solutions, in *Seismological algorithms: Computational methods and computer programs*, edited by D. Doornbos, Academic Press, San Diego, Calif.

Sambridge, M., and K. Mosegaard (2002), Monte Carlo methods in geophysical inverse problems, *Rev. Geophys*, *40*(3), 3–32.

Shapiro, N. M., and M. H. Ritzwoller (2002), Monte-Carlo inversion for a global shear-velocity model of the crust and upper mantle, *Geophys. J. Int.*, *151*(1), 88–105.

Shapiro, N. M., M. H. Ritzwoller, P. H. Molnar, and V. Levin (2004), Thinning and flow of Tibetan crust constrained by seismic anisotropy, *Science*, *305*(5681), 233–236.

Shapiro, N. M., M. Campillo, L. Stehly, and M. H. Ritzwoller (2005), High resolution surface wave tomography from ambient seismic noise, *Science*, *307(5715)*, 1615-1618, 11 March 2005.

Snelson, C. M., T. J. Henstock, G. R. Keller, K. C. Miller, and A. Levander (1998), Crustal and uppermost mantle structure along the Deep Probe seismic profile, *Rocky Mountain Geology*, *33*(2), 181–198.

Snieder, R. K. (1988), Large-scale waveform inversions of surface waves for lateral heterogeneity 1. Theory and numerical examples, *J. Geophys. Res.*, *93*(B10), 12,055–12,065.

Tanimoto, T., and D. L. Anderson (1984), Mapping convection in the mantle, *Geophys. Res. Lett.*, *11*(4), 287–290.

Tarantola, A., and B. Valette (1982), Generalized nonlinear inverse problems solved using the least squares criterion, *Rev. Geophys. Space Phys*, *20*(2), 219–232.

Thurber, C., H. Zhang, F. Waldhauser, J. Hardebeck, A. Michael, and D. Eberhart-Phillips (2006), Three-dimensional compressional wavespeed model, earthquake relocations, and focal mechanisms for the Parkfield, California, region, *Bull. Seis. Soc. of Am.*, *96*(4 B), 38–49.

Trampert, J., and J. H. Woodhouse (1996), High resolution global phase velocity distributions, *Geophys. Res. Lett.*, *23*(1), 21–24.

van der Lee, S. (2002), High-resolution estimates of lithospheric thickness from Missouri to Massachusetts, USA, *Earth Plan. Sci. Lett.*, *203*(1), 15–23.

van der Lee, S., and A. Frederiksen (2005), Surface wave tomography applied to the North American upper mantle, *Geophysical monograph*, *157*, 67–80.

van der Lee, S., and G. Nolet (1997), Upper mantle S velocity structure of North America, *J. Geophys. Res.*, *102*(B10), 22,815–22,838.

Villaseñor, A., M. H. Ritzwoller, A. L. Levshin, M. P. Barmin, E. R. Engdahl, W. Spakman, and J. Trampert (2001), Shear velocity structure of central Eurasia from inversion of surface wave velocities, *Phys. Earth Planet. Inter*, *123*(1), 169–184.

Weeraratne, D. S., D. W. Forsyth, K. M. Fischer, and A. A. Nyblade (2003), Evidence for an upper mantle plume beneath the Tanzanian craton from Rayleigh wave tomography, *J. Geophys. Res.*, *108*(B9), 2427–2446.

Wernicke, B. P., G. J. Axen, and J. K. Snow (1988), Basin and Range extensional tectonics at the latitude of Las Vegas, Nevada, *Bull. Geol. Soc. Am.*, *100*(11), 1738–1757.

Wilson, C. K., C. H. Jones, and H. J. Gilbert (2003), Single-chamber silicic magma system inferred from shear wave discontinuities of the crust and uppermost mantle, coso geothermal area, California, *J. Geophys. Res*, *108*, 1–16.

Yang, Y. and D.W. Forsyth (2006), Rayleigh wave phase velocities, small-scale convection, and azimuthal anisotropy beneath Southern California, *J. Geophys. Res*, *111*, B07306, doi:10.1029/2005JB004180.

Yang, Y., M. H. Ritzwoller, A. L. Levshin, and N. M. Shapiro (2007a), Ambient noise Rayleigh wave tomography across Europe, *Geophys. J. Int.*, *168*(1), 259–274.

Yang, Y., A. Li, and M.H. Ritzwoller (2008), Crustal and uppermost mantle structure in southern Africa revealed from ambient noise and teleseismic tomography, *Geophys. J. Int., 174(1)*, 235-248.

Yao, H., R. D. van der Hilst, and M. V. de Hoop (2006), Surface-wave array tomography in SE Tibet from ambient seismic noise and two-station analysis-I. Phase velocity maps, *Geophys. J. Int.*, *166*(2), 732–744.

Yao H., Beghein, C., and Van der Hilst, R.D., Surface-wave array tomography in SE Tibet from ambient seismic noise and two-station analysis: II Crustal and upper mantle structure, *Geophys. J. Int.*, *173(1)*, 205-219, doi:10.1111/j.1365-246X.2007.03696.x.

Yuan, H., and K. Dueker (2005), Upper mantle tomographic Vp and Vs images of the Rocky Mmountains in Wyoming, Colorado and New Mexico: Evidence for a thick heterogeneous chemical lithosphere, *Geophysical Monograph*, *154*, 329–345.

Table 1. χ^2 misfit for Rayleigh and Love waves averaged from 8 to 20 sec period across Nevada. Column 1 lists the method of crustal model parameterization, where "Monotonic Isotropic" denotes 3 crustal layers of monotonically increasing isotropic velocity with depth, "Nonmonotonic Isotropic" is also isotropic but with the monotonicity constraint removed for 4 crustal layers, and "Radial Anisotropy" is where radial anisotropy is allowed in the middle of the 3 crustal layers. Columns 2, 3, and 4 indicate χ^2 values for Love wave phase speed, Rayleigh wave phase speed, and the average of the two. The final column lists the variance reduction over the monotonic isotropic parameterization.

Param. type	χ^2-Love	χ^2-Rayleigh	χ^2-avg.	Variance Reduction
Monotonic Isotropic	2.21	1.42	1.81	
Nonmonotonic Isotropic	1.45	1.63	1.54	15.2%
Radial Anisotropy	1.05	1.07	1.06	41.6%

Figure 1. Map of the study area showing stations used in the experiment as black triangles. Grey circles, squares, and a star are the locations for the examples in Figures 6, 7, 8, and 17.

Figure 2. Regions and geographic features. The black contour surrounds the area with lateral resolution better than 500 km for the 16 s Rayleigh wave phase velocity. Tectonic provinces are outlined in red and are labeled (bounded by rectangles) for reference. Features (from east to west) are as follows: Appalachian Highlands(ApH), Ouachita-Ozark Highlands (OH), Central Lowlands (CL), Great Plains (GP), Rocky Mountain Region (RM), Colorado Plateau (CP), Basin and Range (B&R), Columbia Plateau (CP), Sierra Nevada Mountains (SN), and Great Valley (GV). Other features are labeled (bounded by ellipses) as follows: Appalachian Basin (ApB), Michigan Basin (MB), Mississippi Embayment (ME), Mid-continental Rift (MCR), Anadarko Basin (AB), Williston Basin (WB), Rio Grande Rift (RGR), Green River Basin (GRB), Gulf of California (GC), and Pacific Northwest (PNW).

Figure 3. Sensitivity kernels for Rayleigh (labeled RC) and Love (labeled LC) wave phase speeds at a selection of periods.

Figure 4. Spatially averaged uncertainty across the Rayleigh wave group and phase speed and the Love wave phase speed maps. These are the average values within which we attempt to fit the data.

Figure 5. An illustration of the parameterization of the models used to create dispersion curves for (a) the linearized inversion and (b) the Monte-Carlo inversion. Fifteen layers are used in the mantle for the linearized inversion while five B-splines are used in the mantle for the Monte-Carlo inversion.

Figure 6. Example of the best fitting model and dispersion curves from the linearized inversion for a point in Illinois. Rayleigh and Love wave phase speed measurements and uncertainties are represented with error bars in (a). The input model in (b) and related dispersion curves in (a) are shown as grey dashed lines. The estimated models and dispersion curves are thin black lines in (b) and (a). The latitude, longitude and approximate location is listed in (b) and labeled as a grey circle in Figure 1. Velocity values at the center of each mantle layer are plotted.

Figure 7. Same as Figure 6 but for points in California and Montana, shown as grey circles in Figure 1. The χ^2 value indicated in (c) is toward the larger end in this study.

Figure 8. Examples of the input and output dispersion curves (error bars and grey lines, respectively, in (b), (d), and (f)) and the resulting ensemble of Monte-Carlo models ((a), (c), and (e)). The "favored model" is drawn in red. Locations of the examples presented here are shown as grey squares in Figure 1.

Figure 9. Representation of the short-period discrepancy between Rayleigh and Love waves from the isotropic "favored models" that emerge from the Monte Carlo inversion. The difference of the model predicted and measured wave speed is divided by the data error at each point for each period. The results presented here are the average of values from 8 - 20 s period. Greens/oranges indicate that the model is too fast and blues that the model is too slow.

Figure 10. A selection of horizontal V_s depth sections through the isotropic "favored model" from Monte-Carlo inversion. Panels (c) and (d) show the model at 4 km above and below the recovered Moho, respectively.

Figure 11. The crustal thickness of the "favored model" from the Monte-Carlo inversion. Crustal thickness is required to be within 5 km of the values of *Bassin et al.* [2000].

Figure 12. A selection of V_s vertical cross sections through the "favored model" from Monte-Carlo inversion. The locations of the cross-sections are indicated in (a) and the horizontal scale of all the cross-sections is the same. The recovered Moho is plotted in all cross-sections as a black line. Different color scales are used in the crust and mantle, as shown at bottom.

Figure 13. (a) The average standard deviation of the ensemble of models from the Monte Carlo inversion is plotted versus depth as the solid line. The dashed line is the mean of the absolute value of the velocity anomalies at each depth taken across the entire study region. (b) The standard deviation of the dispersion curves predicted by the ensemble of models averaged across all geographic points is shown.

Figure 14. Horizontal slices showing the estimated standard deviation of the ensemble of V_s models derived from the Monte-Carlo inversion at the depths presented in Figure 10. Panels (c) and (d) are results at 4 km above and below the Moho, respectively.

Figure 15. Histograms of velocity values taken from the 0.5° grid east and west of the approximate location of the boundary of the crustal dichotomy in the lower crust and at 80 km depth across the profile at 40°N. The values are from the "favored model" and the boundary is defined at 3.75 and 4.55 km/s in the lower crust and mantle, respectively.

Figure 16. The location and uncertainty in the east-west shear velocity dichotomy for the lower crust (a) and the uppermost mantle (b). Contours of velocity are plotted for the 20th (grey) and 80th (black) percentile models at 3.75 km/s for the lower crust and 4.55 at 80 km in the mantle taken from the ensemble of accepted models determined by Monte Carlo inversion. The red contour marks the approximate location of the Rocky Mountain Front.

Figure 17. An example of the improvement in fit afforded by allowing radial anisotropy or breaking the monotonicity constraint (allowing a low velocity zone, LVZ) in the crust. The dispersion curves for the monotonic isotropic, radial anisotropic, and LVZ model are labeled in (a) and the corresponding models are shown in (b). Radial anisotropy is allowed only in the middle crust.

Figure 18. (a) The best fitting middle crustal radial anisotropy model for the US where, for example, a value of 5% signifies $Vsh/Vsv = 1.05$. (b) The minimally anisotropic model from the ensemble of acceptable models that emerge from the Monte-Carlo inversion.

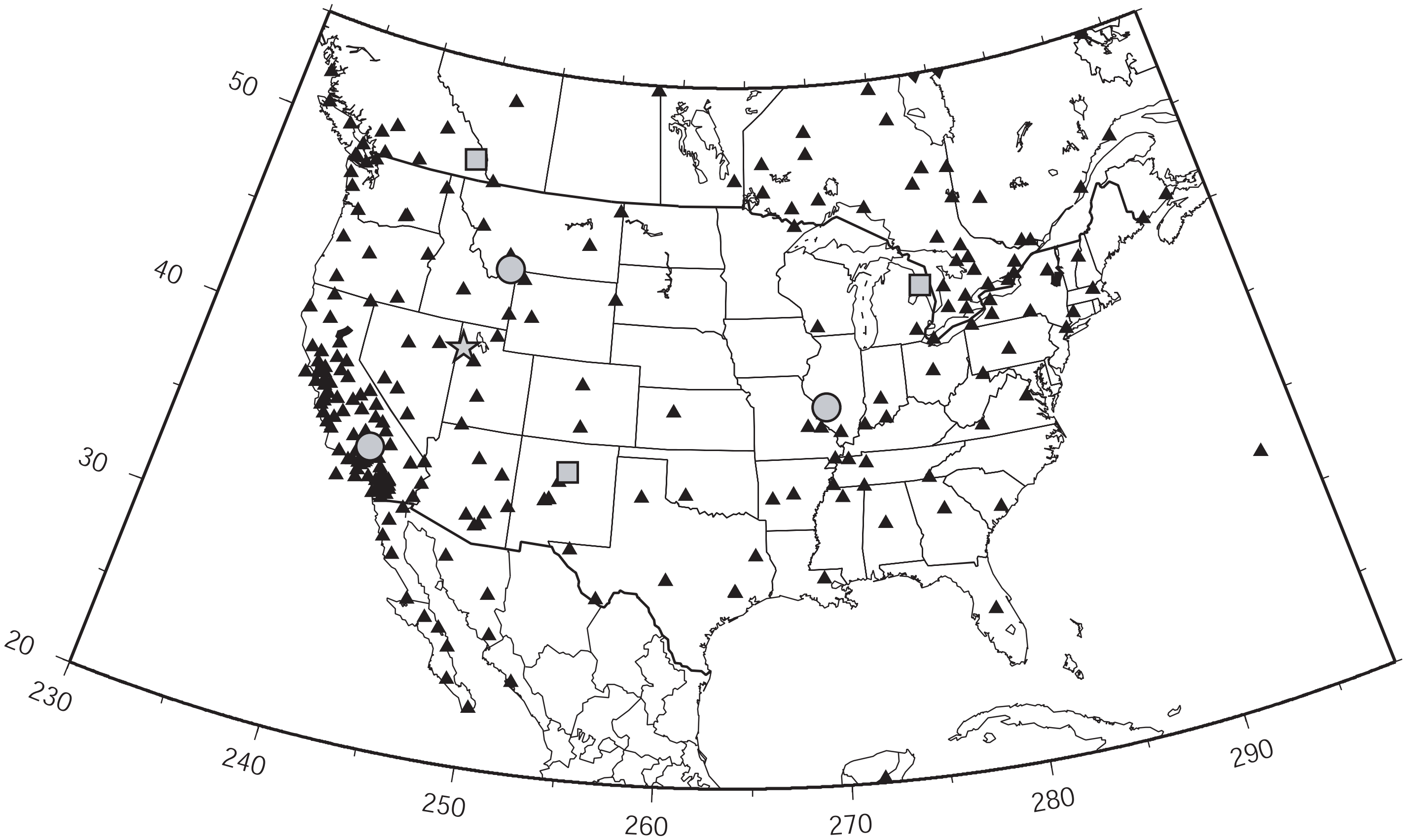
50
40
30
20
230
240
250
260
270
280
290

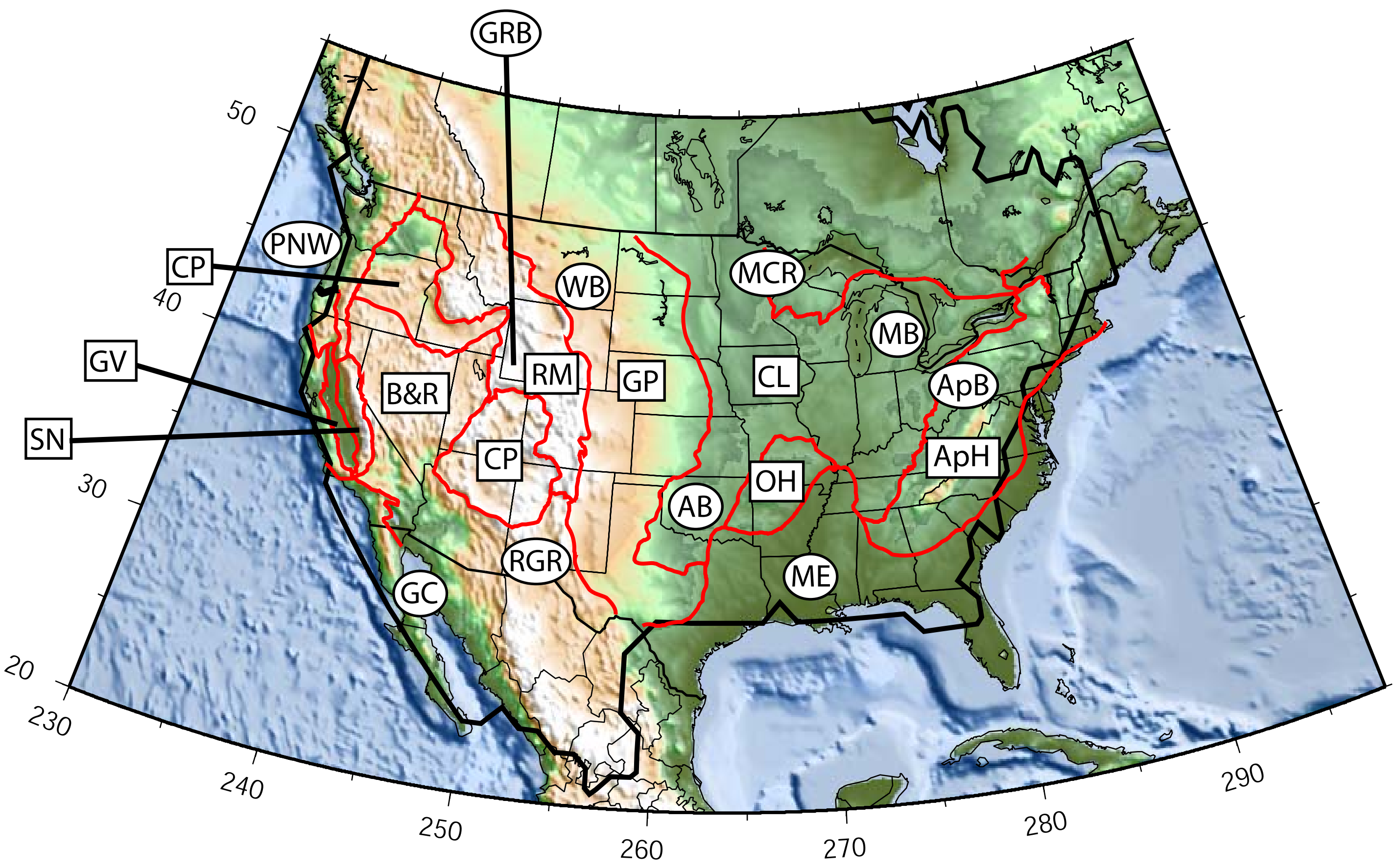
GRB
50
PNW
CP
WB
MCR
40
GV
B&R
RM
GP
CL
MB
ApB
SN
CP
ApH
30
OH
AB
RGR
ME
GC
20
230
240
250
260
270
280
290

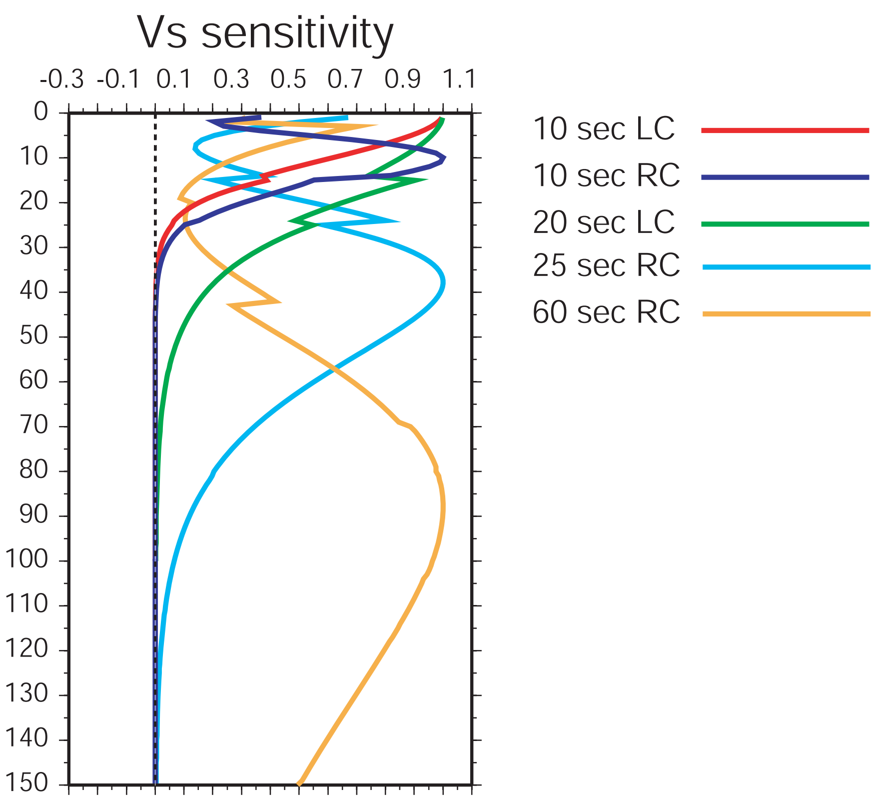
Vs sensitivity
-0.3 -0.1 0.1 0.3 0.5 0.7 0.9 1.1
0
10
20
30
40
50
60
70
80
90
100
110
120
130
140
150
10 sec LC
10 sec RC
20 sec LC
25 sec RC
60 sec RC

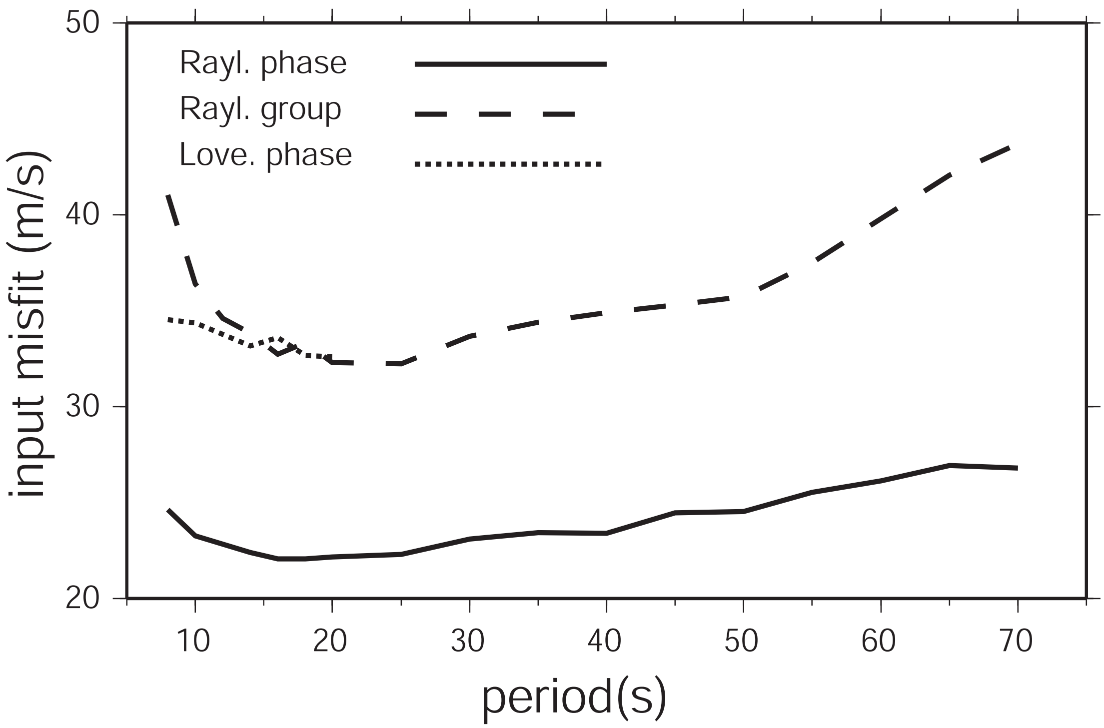
Rayl. phase
Rayl. group
Love. phase
input misfit (m/s)
period(s)
50
40
30
20
10
20
30
40
50
60
70

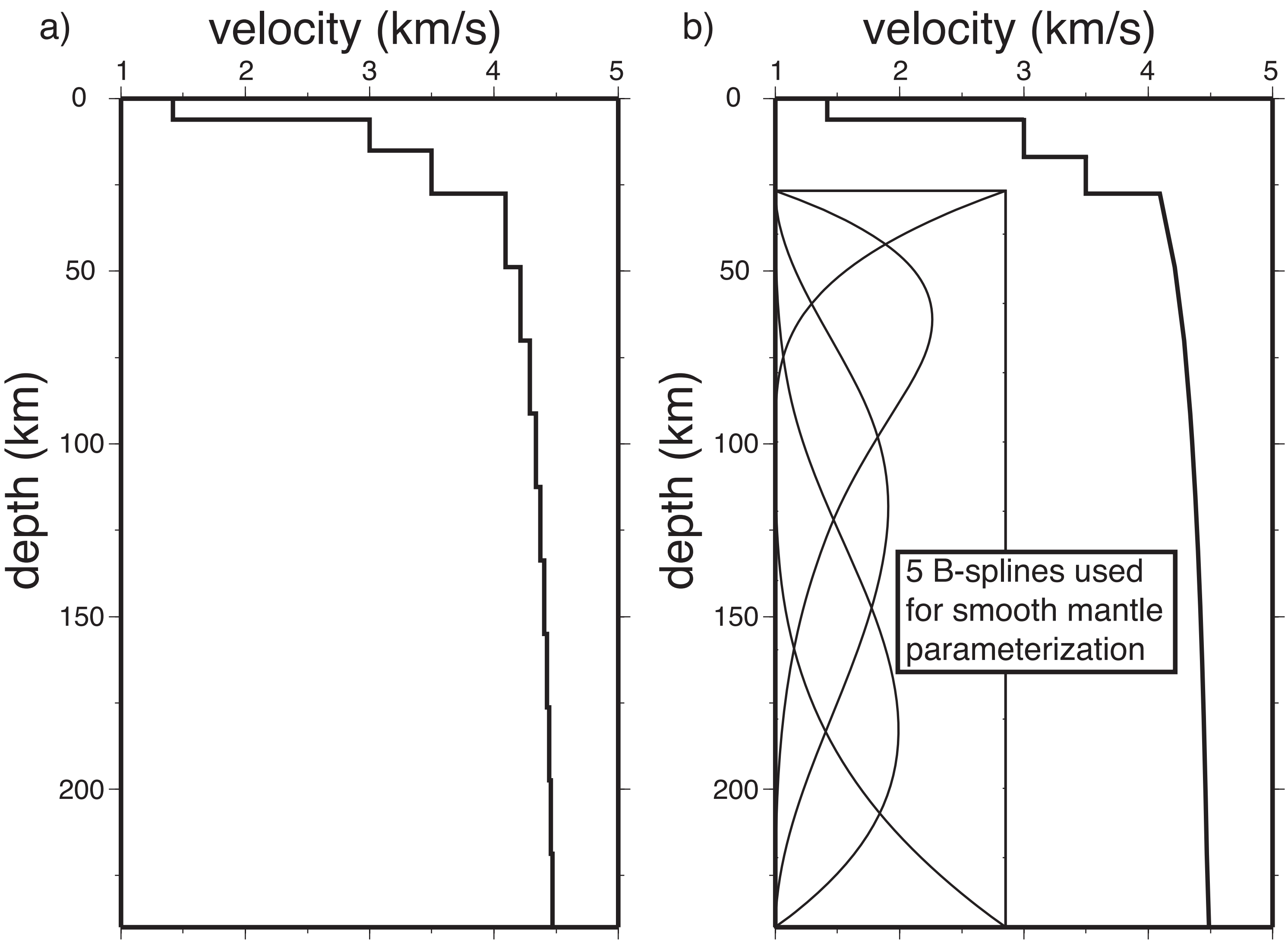
a)
velocity (km/s)
1
2
3
4
5
0
50
100
150
200
depth (km)
b)
velocity (km/s)
1
2
3
4
5
0
50
100
150
200
depth (km)
5 B-splines used
for smooth mantle
parameterization

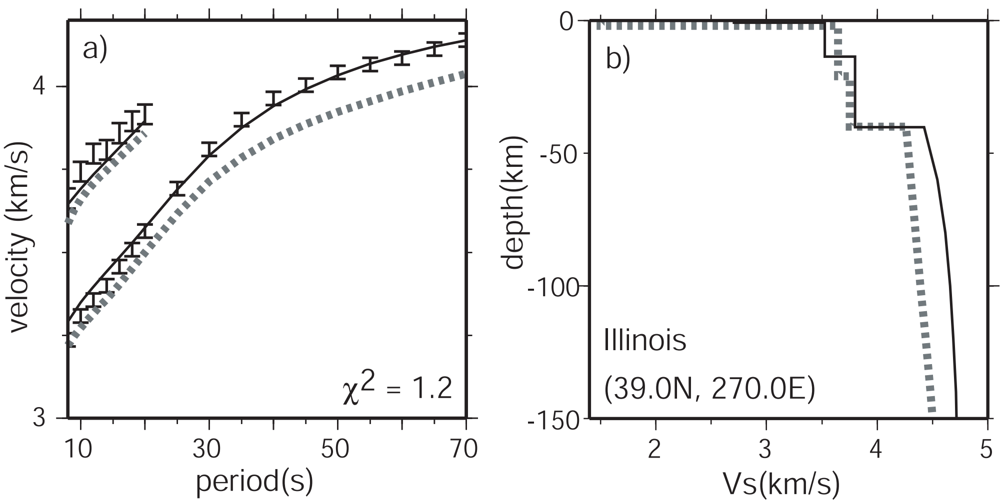

a)
velocity (km/s)
period(s)
χ^2 = 1.2
b)
depth(km)
Vs(km/s)
Illinois
(39.0N, 270.0E)

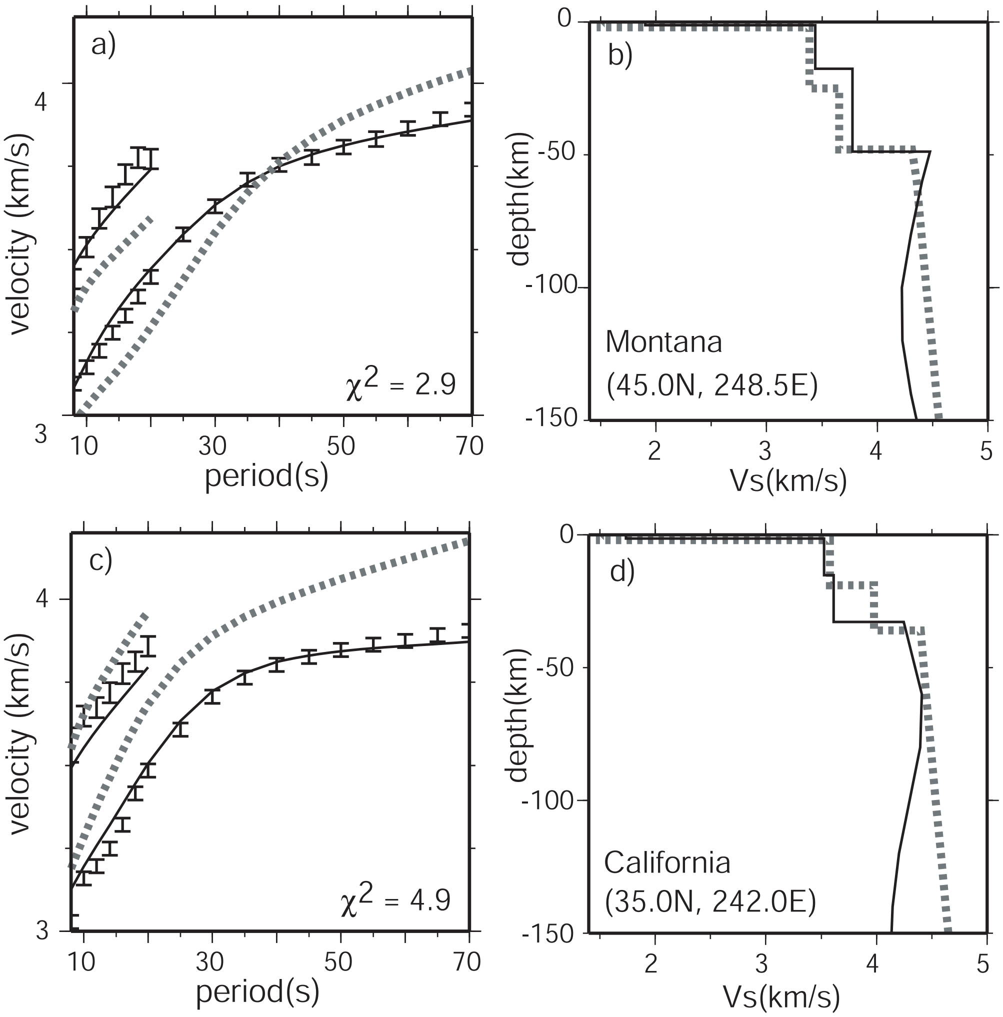
a)
b)
c)
d)
velocity (km/s)
period(s)
depth(km)
Vs(km/s)
χ^2 = 2.9
χ^2 = 4.9
Montana
(45.0N, 248.5E)
California
(35.0N, 242.0E)

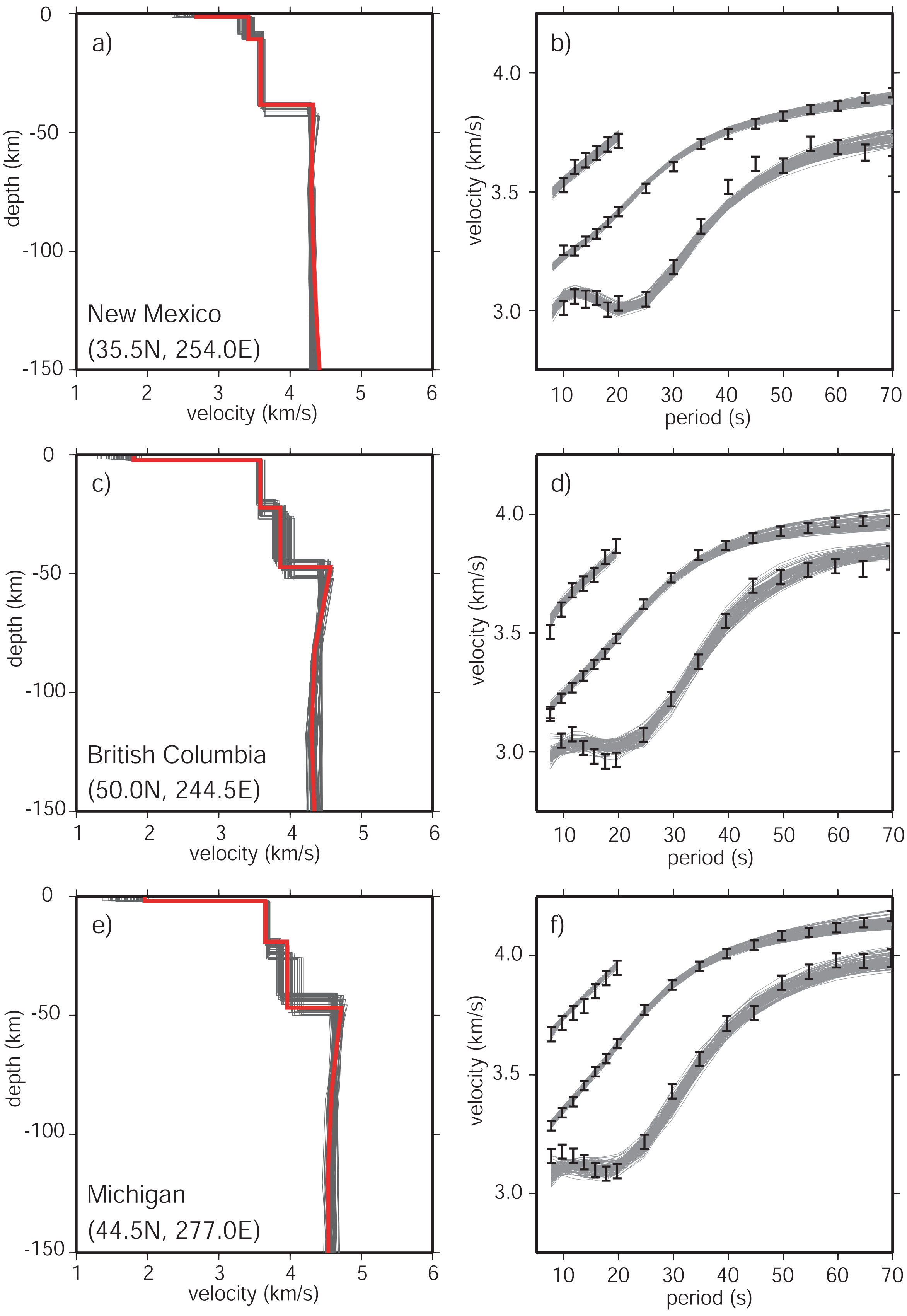

a)
New Mexico
(35.5N, 254.0E)
b)
c)
British Columbia
(50.0N, 244.5E)
d)
e)
Michigan
(44.5N, 277.0E)
f)
depth (km)
velocity (km/s)
period (s)

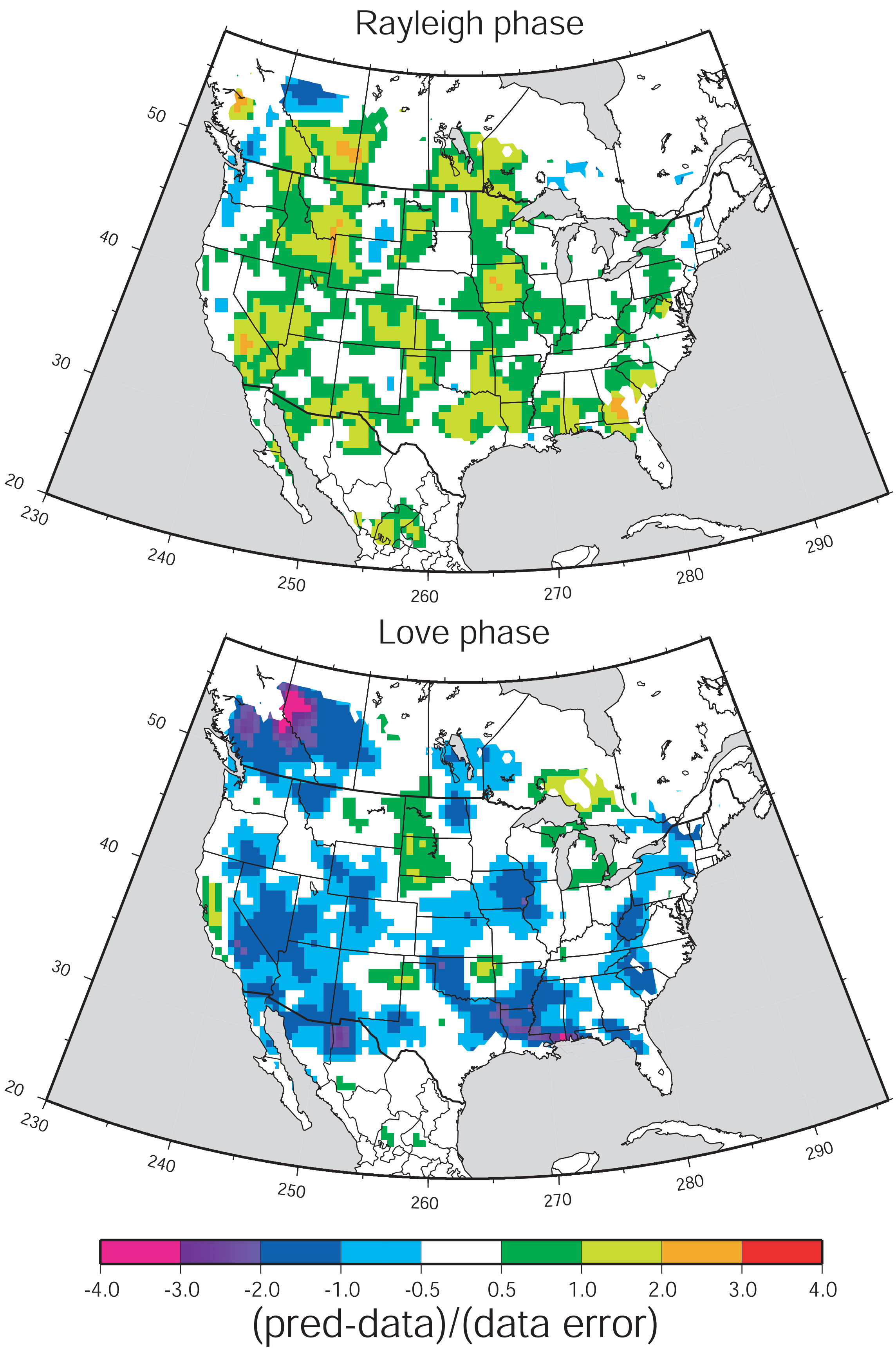
Rayleigh phase
50
40
30
20
230
240
250
260
270
280
290
Love phase
50
40
30
20
230
240
250
260
270
280
290
-4.0
-3.0
-2.0
-1.0
-0.5
0.5
1.0
2.0
3.0
4.0
(pred-data)/(data error)

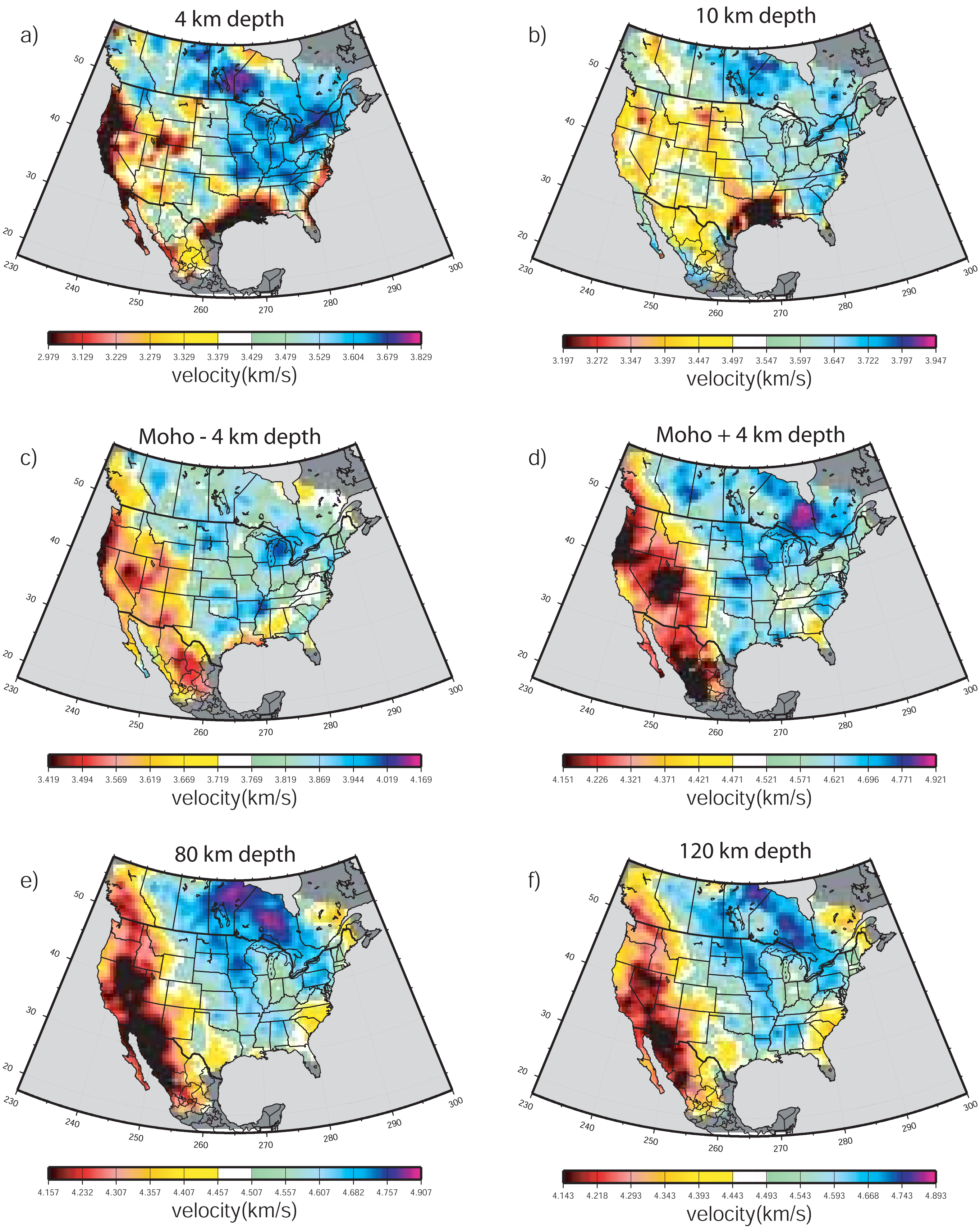
a)
4 km depth
2.979 3.129 3.229 3.279 3.329 3.379 3.429 3.479 3.529 3.604 3.679 3.829
velocity(km/s)
b)
10 km depth
3.197 3.272 3.347 3.397 3.447 3.497 3.547 3.597 3.647 3.722 3.797 3.947
velocity(km/s)
c)
Moho - 4 km depth
3.419 3.494 3.569 3.619 3.669 3.719 3.769 3.819 3.869 3.944 4.019 4.169
velocity(km/s)
d)
Moho + 4 km depth
4.151 4.226 4.321 4.371 4.421 4.471 4.521 4.571 4.621 4.696 4.771 4.921
velocity(km/s)
e)
80 km depth
4.157 4.232 4.307 4.357 4.407 4.457 4.507 4.557 4.607 4.682 4.757 4.907
velocity(km/s)
f)
120 km depth
4.143 4.218 4.293 4.343 4.393 4.443 4.493 4.543 4.593 4.668 4.743 4.893
velocity(km/s)

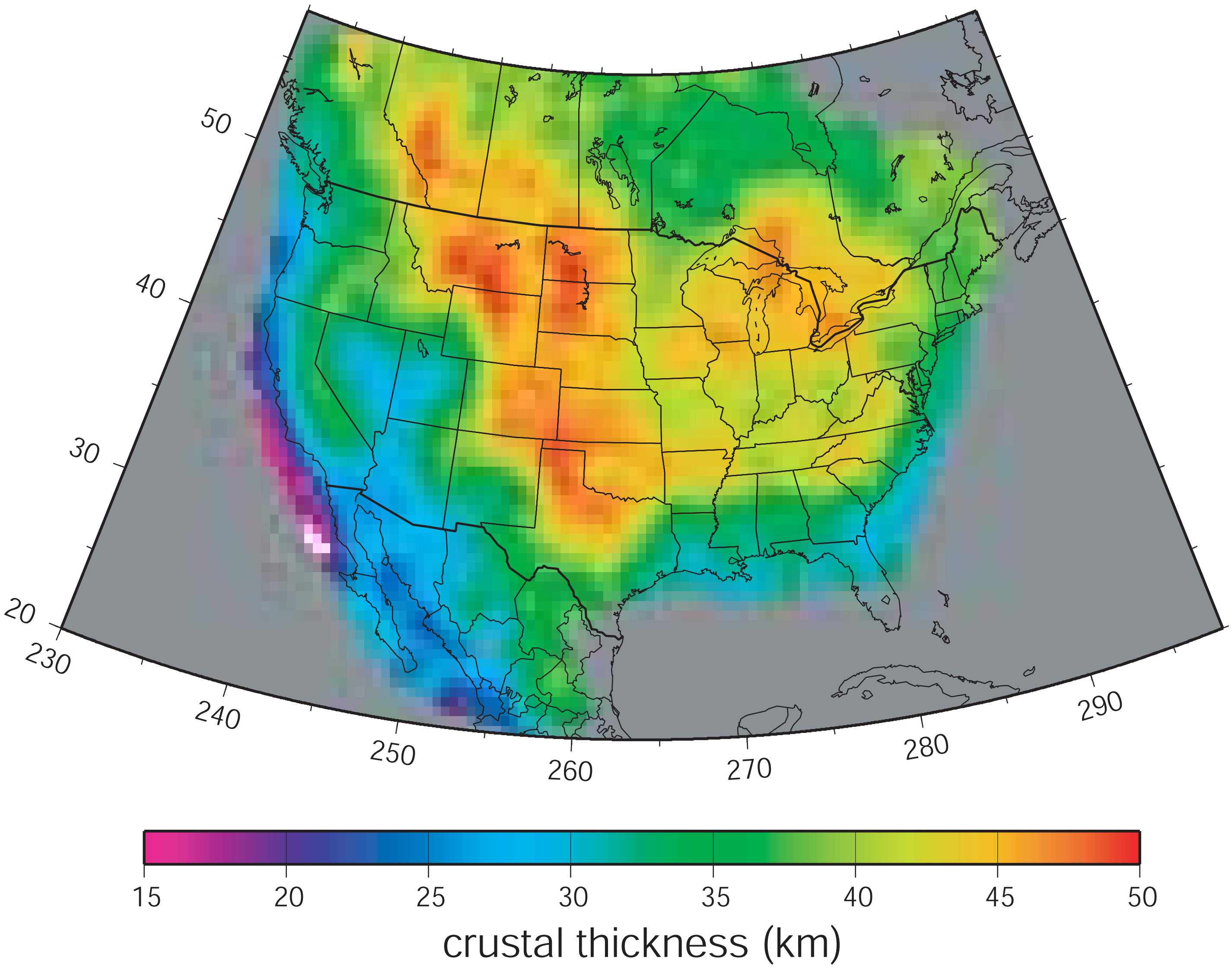

50
40
30
20
230
240
250
260
270
280
290
15
20
25
30
35
40
45
50
crustal thickness (km)

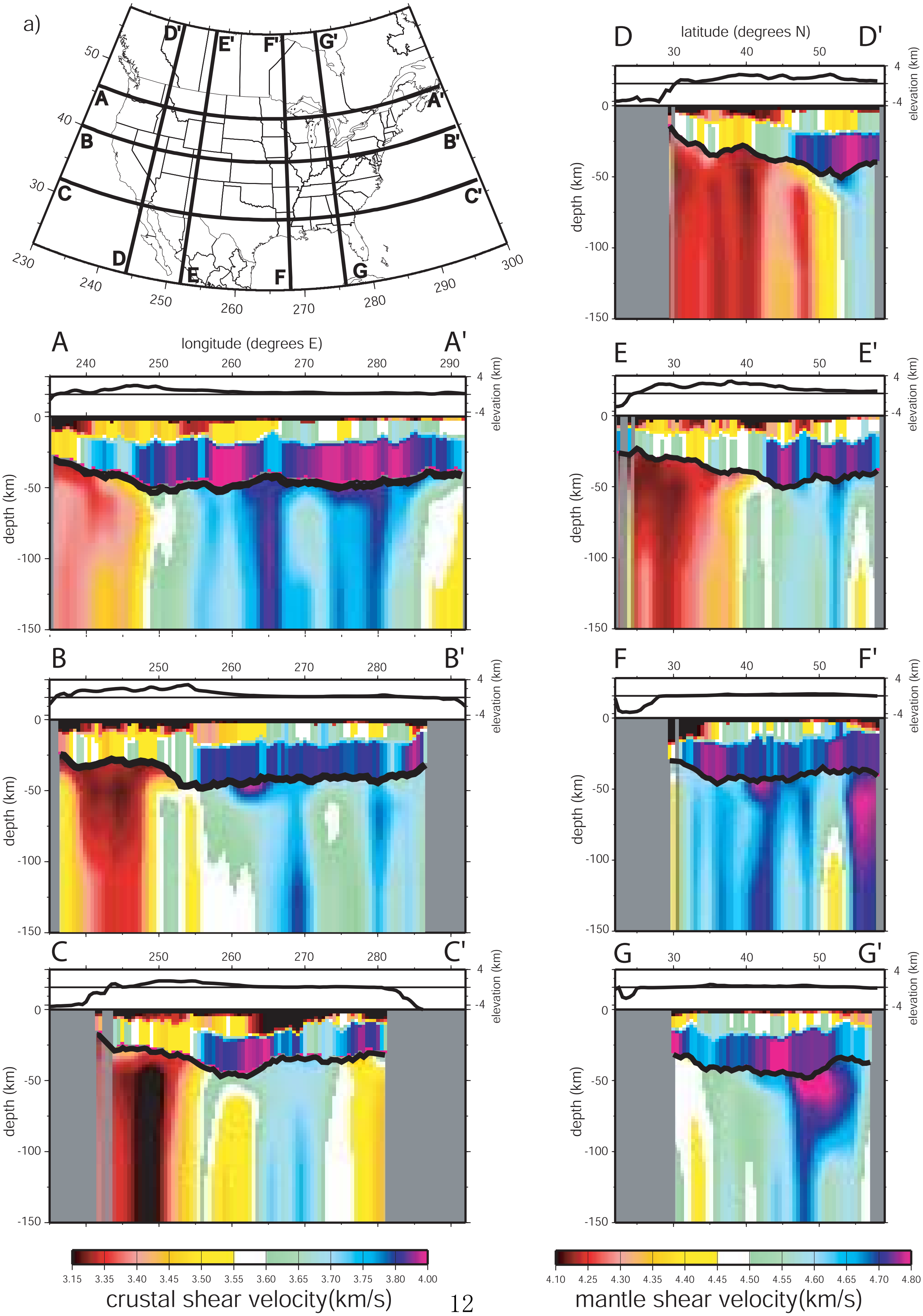

a)
D D' E E' F F' G G'
A A' B B' C C'
230 240 250 260 270 280 290 300
30 40 50
longitude (degrees E)
latitude (degrees N)
depth (km)
elevation (km)
crustal shear velocity(km/s)
3.15 3.35 3.40 3.45 3.50 3.55 3.60 3.65 3.70 3.75 3.80 4.00
mantle shear velocity(km/s)
4.10 4.25 4.30 4.35 4.40 4.45 4.50 4.55 4.60 4.65 4.70 4.80

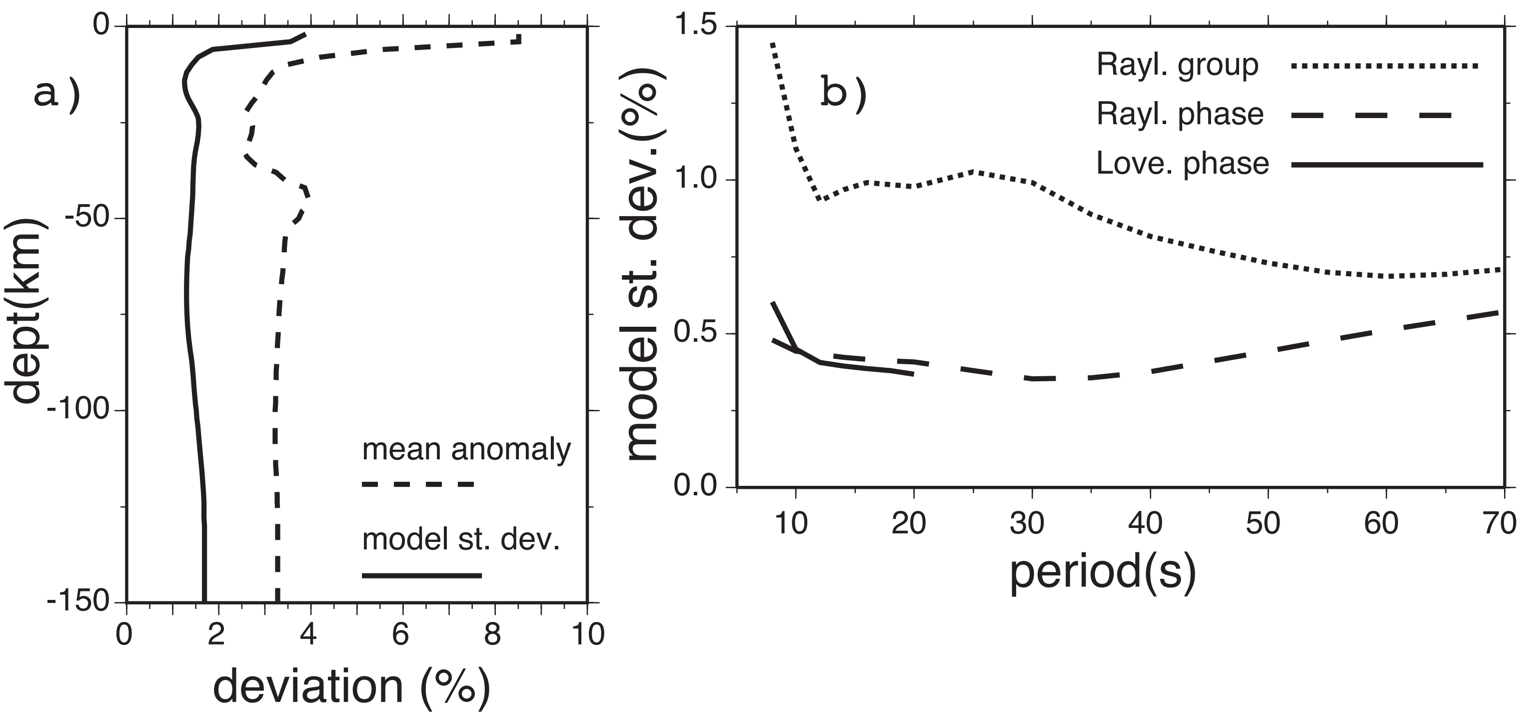
a)
0
-50
-100
-150
dept(km)
0
2
4
6
8
10
deviation (%)
mean anomaly
model st. dev.
b)
1.5
1.0
0.5
0.0
model st. dev.(%)
10
20
30
40
50
60
70
period(s)
Rayl. group
Rayl. phase
Love. phase

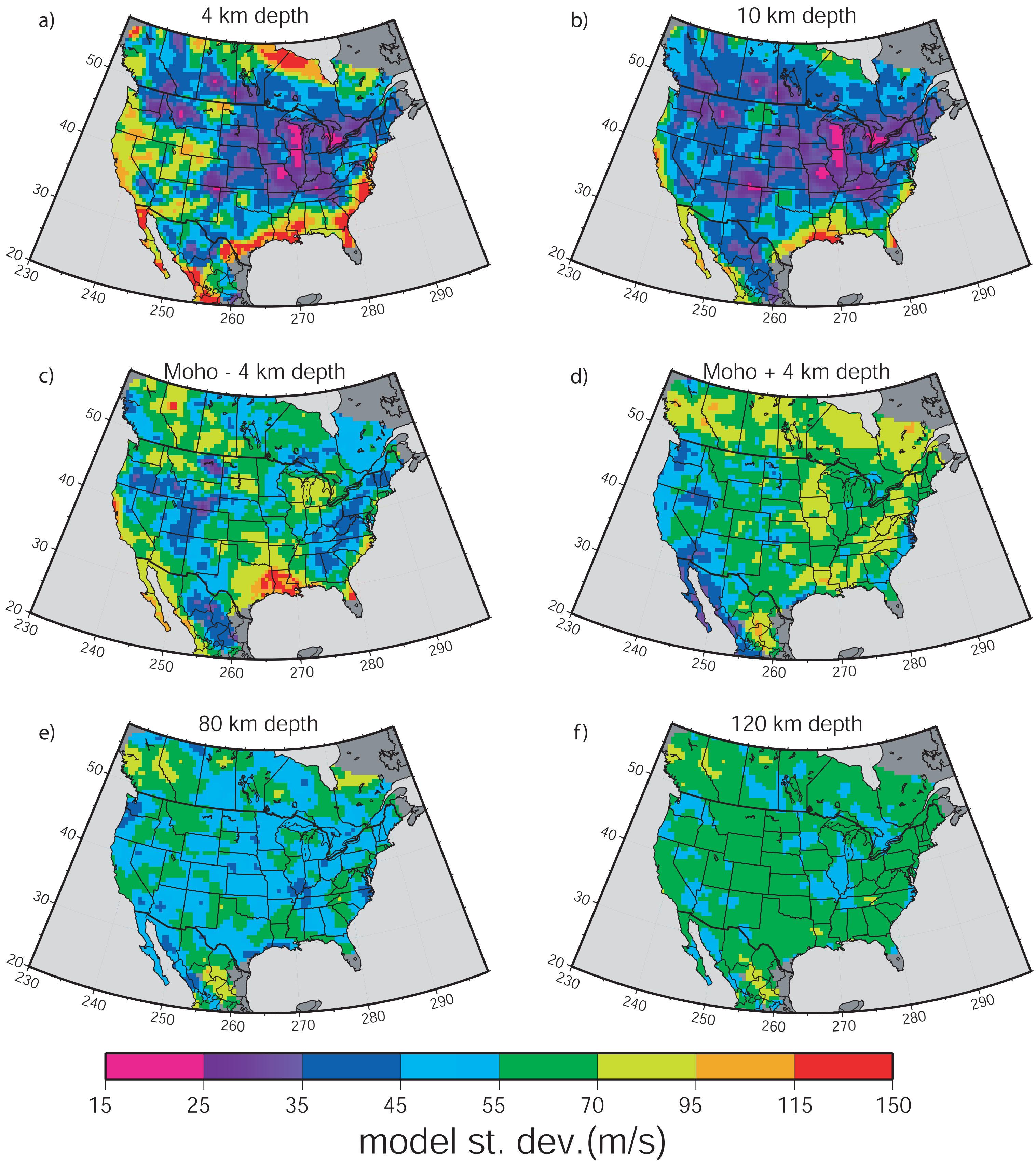

a)
4 km depth
b)
10 km depth
c)
Moho - 4 km depth
d)
Moho + 4 km depth
e)
80 km depth
f)
120 km depth
20
30
40
50
230
240
250
260
270
280
290
15
25
35
45
55
70
95
115
150
model st. dev.(m/s)

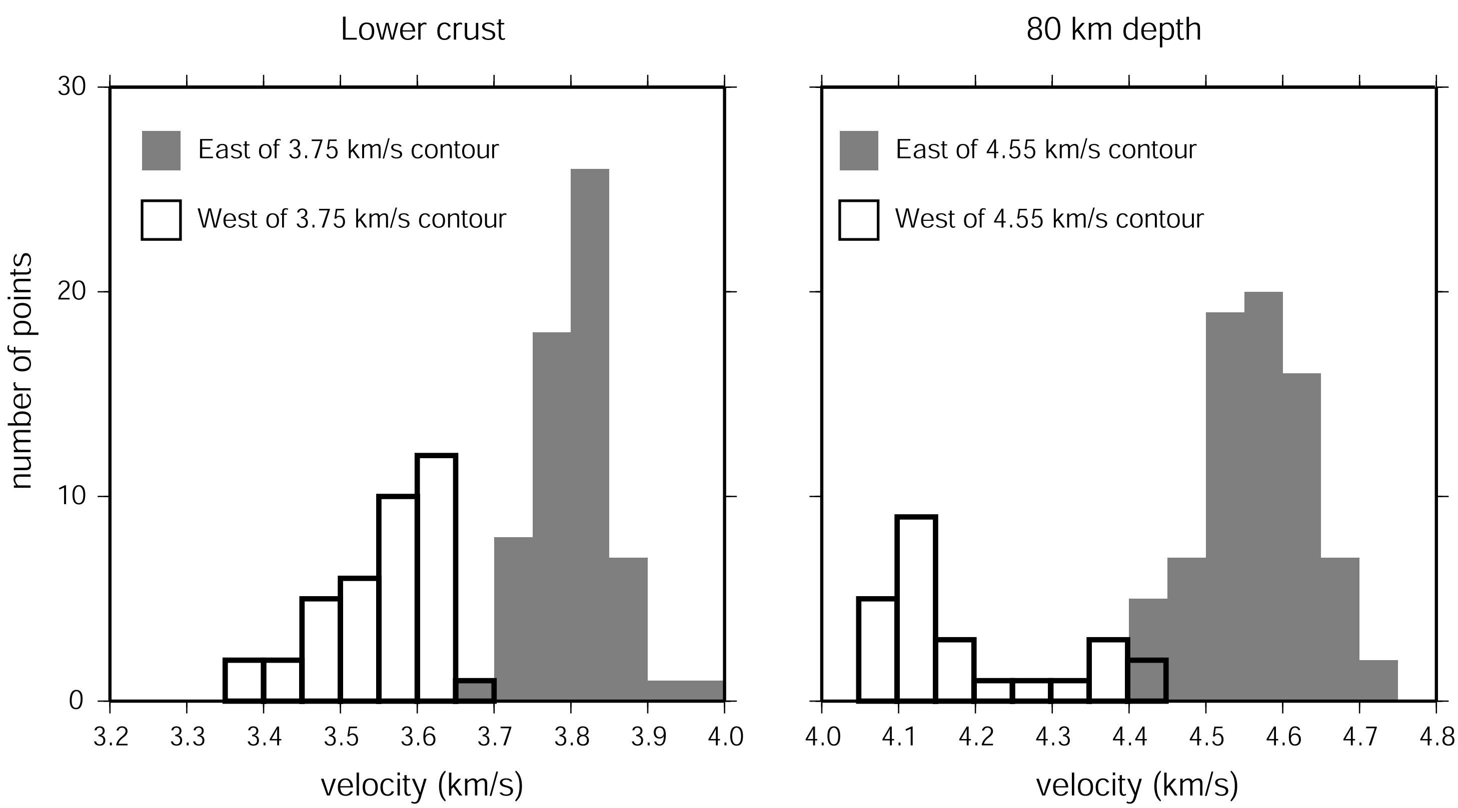
Lower crust
80 km depth
number of points
East of 3.75 km/s contour
West of 3.75 km/s contour
East of 4.55 km/s contour
West of 4.55 km/s contour
0
10
20
30
3.2
3.3
3.4
3.5
3.6
3.7
3.8
3.9
4.0
4.1
4.2
4.3
4.4
4.5
4.6
4.7
4.8
velocity (km/s)
velocity (km/s)

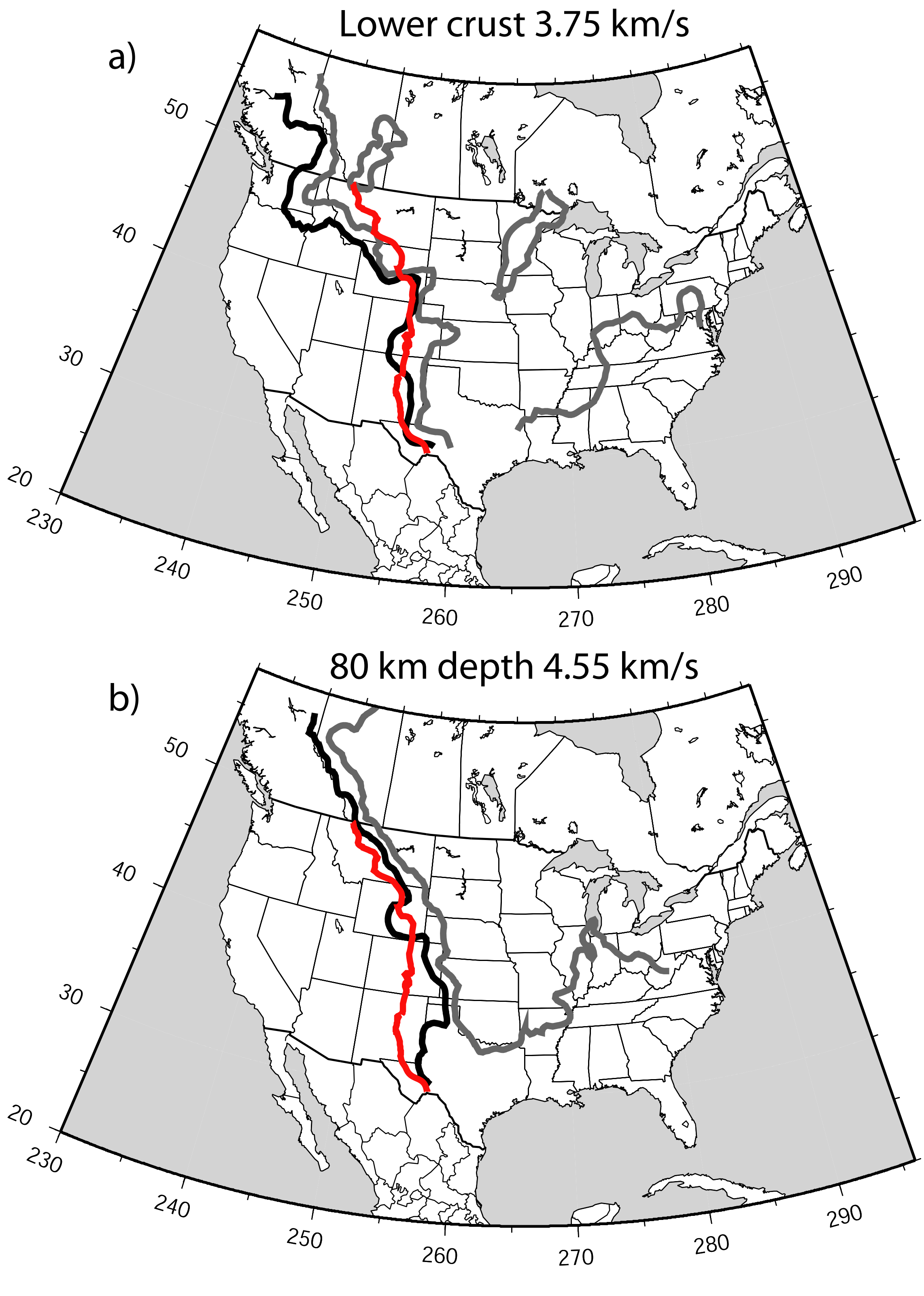

a)
Lower crust 3.75 km/s
50
40
30
20
230
240
250
260
270
280
290
b)
80 km depth 4.55 km/s
50
40
30
20
230
240
250
260
270
280
290

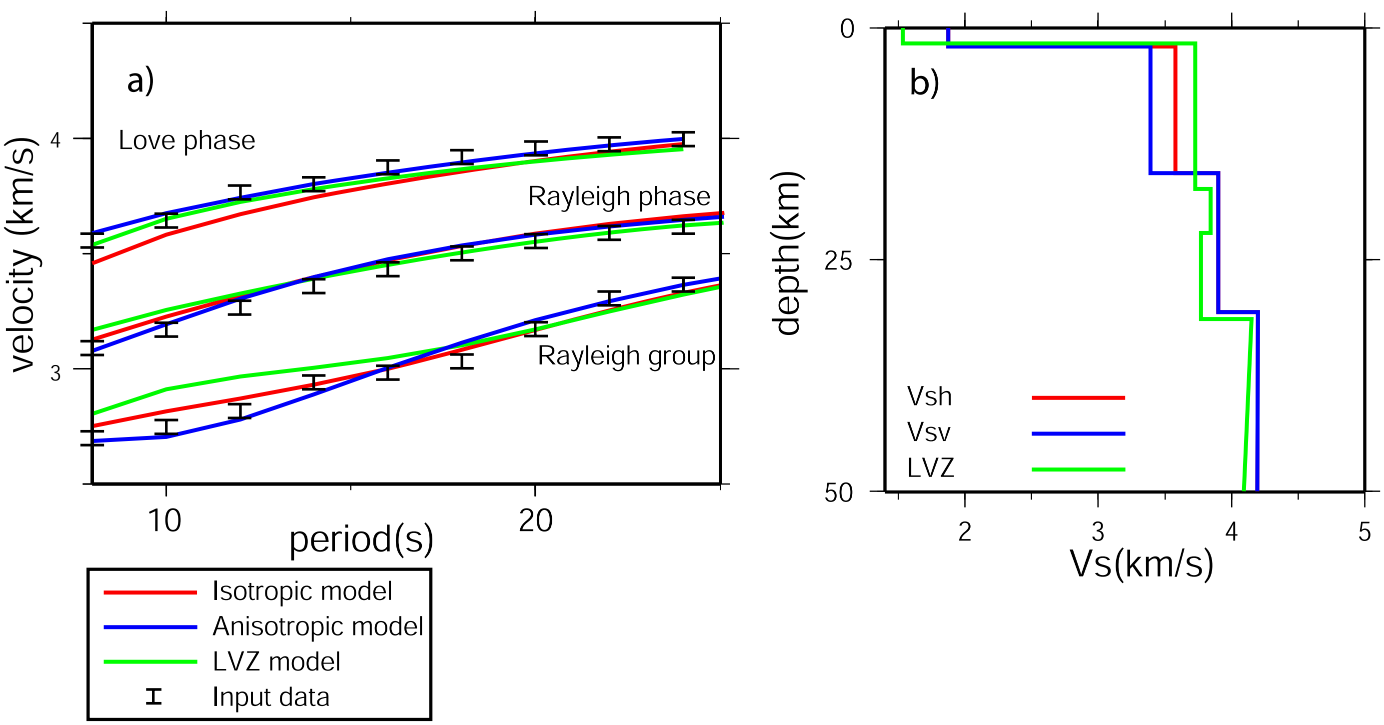

a)
Love phase
Rayleigh phase
Rayleigh group
velocity (km/s)
4
3
10
20
period(s)
Isotropic model
Anisotropic model
LVZ model
Input data
b)
0
25
50
depth(km)
Vsh
Vsv
LVZ
2
3
4
5
Vs(km/s)

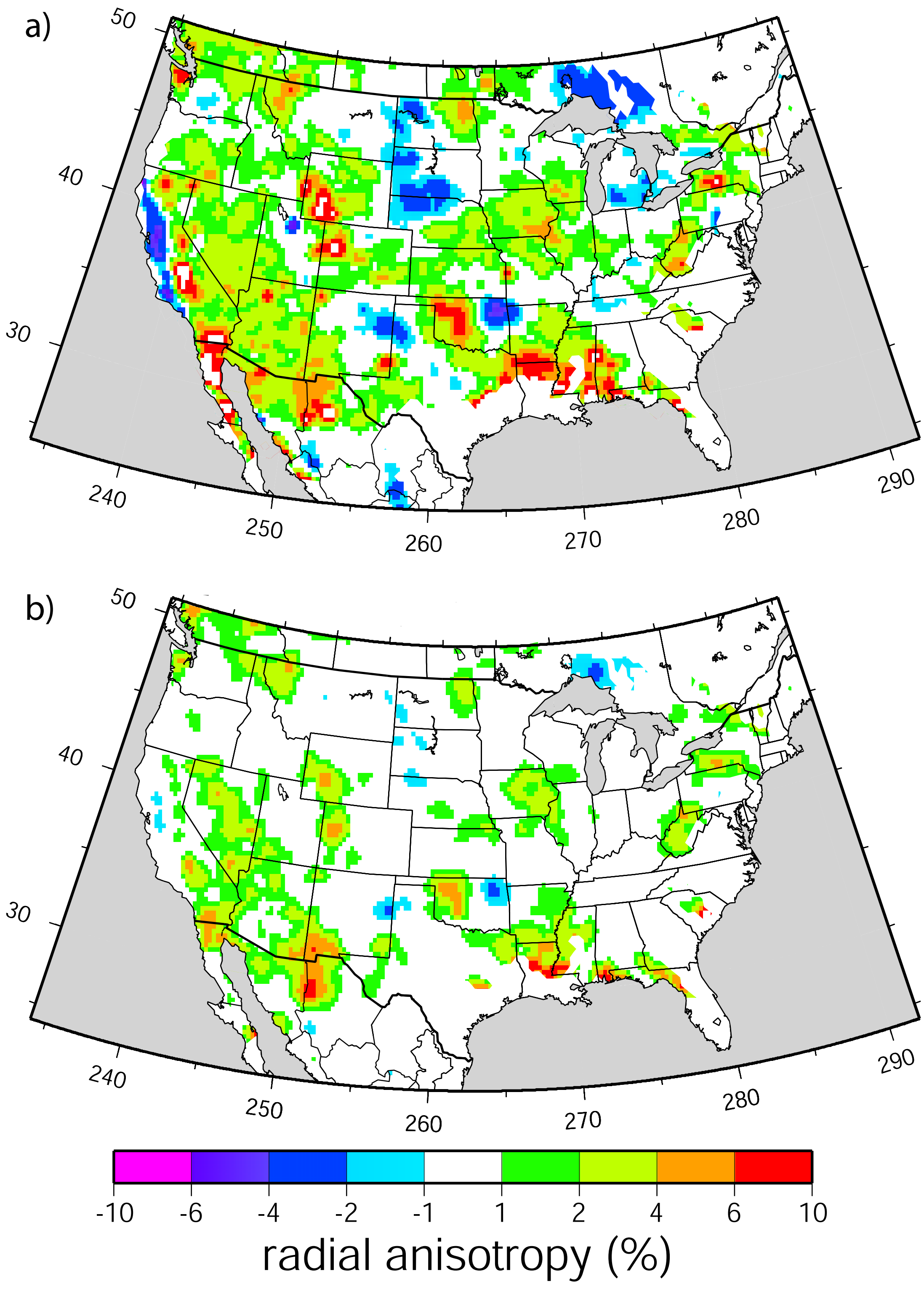
a)
b)
50
40
30
240
250
260
270
280
290
-10
-6
-4
-2
-1
1
2
4
6
10
radial anisotropy (%)